International Journal of Plasticity 182 (2024) 104118

Contents lists available at ScienceDirect

International Journal of Plasticity

journal homepage: www.elsevier.com/locate/ijplas

Atomistic analysis of the mechanisms underlying irradiation-hardening in Fe–Ni–Cr alloys

A. Ustrzycka [a,*], F.J. Dominguez-Gutierrez [b], W. Chromiński [b,c]

[a] Institute of Fundamental Technological Research, Polish Academy of Sciences, Pawinskiego 5B, Warsaw, 02-106, Poland
[b] NOMATEN Centre of Excellence, National Centre for Nuclear Research, ul. A. Soltana 7, Otwock, 05-400, Poland
[c] Warsaw University of Technology, Faculty of Materials Science and Engineering, Woloska 141, Warsaw, Poland

ARTICLE INFO

Keywords:
Radiation-induced defects
Irradiation hardening
Collision cascades
MD simulations
Radiation defects evolution
Cr-rich alloys

ABSTRACT

This work presents a comprehensive examination of the physical mechanisms driving hardening in irradiated face-centered cubic FeNiCr alloys. The evolution of irradiation-induced defects during shear deformation is modeled by atomistic simulations through overlapping cascade simulations, where the nucleation and evolution of dislocation loops is validated by transmission electron microscopy images obtained from irradiated FeNiCr alloys using tandem accelerator. The effect of different shear rates on the microstructure of irradiated materials with a specific focus on the changes in the density of voids and dislocation loops induced by irradiation was analyzed. Additionally, the fundamental interaction processes between single irradiation-induced defects contributing to irradiation hardening, such as voids and dislocation loops in the alloy are explained. The analysis at atomic level indicates that both the dislocation loops and the voids exhibit strengthening effects. Furthermore, the nanometric voids are much stronger obstacles than dislocation loops of comparable size. The mechanism of cutting the voids leads to an increase of voids density and thus contributes to an increase in irradiation hardening. The mechanism of collapse of small voids into dislocation loops leads to decrease of voids density and at the same time increase of loops density. The coupling effect between the density of voids and dislocation loops is determined. Finally, the novel, physical mechanisms-based model of irradiation hardening and dislocation-radiation defect reaction kinetics are developed, which consider the mechanisms of void cutting, void shrink and void collapse to dislocation loop.

1. Introduction

Understanding the profound impact of high-energy particle beams on materials, especially in the challenging conditions of nuclear reactors, is paramount for design and operation. This encompasses extreme radiation fluxes, high stresses, and elevated temperatures (Zinkle and Busby, 2009; Zinkle, 2008). The complexity of particle-matter interactions varies with the type and energy of the particles (Nordlund et al., 2018b; Zinkle, 2008). Swift heavy particles, encountering materials, initiate processes leading to intricate defect structures, including dislocation loops, cavities, and stacking-fault tetrahedra (Zhang et al., 2017). This irradiation induces significant alterations in mechanical properties, such as increased yield stress, embrittlement, volumetric swelling, and decreased ductility, primarily due to radiation-induced defects hindering dislocation motion (Vo et al., 2023; Ustrzycka et al., 2020). Notably, the phenomenon of radiation hardening is intricately linked to the atomic-scale mechanisms of interaction between moving dislocations and radiation-induced defects.

* Corresponding author.
E-mail address: austrzyc@ippt.pan.pl (A. Ustrzycka).

https://doi.org/10.1016/j.ijplas.2024.104118
Received 10 February 2024; Received in revised form 9 August 2024
Available online 6 September 2024

The experimental characterization of these interactions proves challenging, given the practically unobservable nature of these processes that occur within the fleeting time frame of collision cascades (typically on the order of 10^{-12} s). As a result, atomistic simulations emerge as a crucial tool for exploring these intricate issues (Wang et al., 2022; Bryukhanov, 2020; Bao et al., 2022b,a; Tsugawa et al., 2022; Yu et al., 2022; Kurpaska et al., 2022; Dominguez-Gutierrez et al., 2024). Delving into the fundamental mechanisms governing material ductility and dislocation dynamics, researchers like Krasnikov and Mayer (2018) have highlighted the importance of considering local stress fluctuations in analyses. Cho et al. (2017) explored the mobility of dislocations at various temperatures and character angles, while Yanilkin et al. (2014) studied dislocation dynamics in an Al–Cu alloy through MD simulations. Additionally, Bryukhanov (2020) investigated the influence of Ni on the mobility of edge dislocations in a Cu–Ni alloy across a wide temperature range (100–1100 K).

Molecular dynamics simulations have proven effective in studying dislocation interactions with inclusions, loops, and voids, elucidating mechanisms like obstacle formation, bowing of dislocations, and their impact on mechanical properties (Tsugawa et al., 2022; Bao et al., 2022a; Osetsky and Bacon, 2003a; Landeiro Dos Reis et al., 2020). It has been explored that the interactions between dislocations and precipitates, presenting obstacles and forming loops, substantiating the Orowan mechanism (Bao et al., 2022a; Tsugawa et al., 2022). Other investigations include screw dislocation interactions with loops, the effect of radiation-induced defects on strain bursts, and the dynamics of dislocation-void interaction (dong Lin et al., 2024; Cui et al., 2017; Liu and Biner, 2008; Bao et al., 2022b; Hayakawa et al., 2019; Yu et al., 2022).

Understanding radiation-induced defects is pivotal for defining mechanical property evolution, making atomic-level simulations indispensable. Efforts in modeling nuclear materials' microstructure evolution are found in the literature, including work hardening and constitutive equations for yield stress (Kocks and Mecking, 2003; Monnet, 2018; Wu et al., 2022). Simplified constitutive relations for irradiation hardening, focusing on crystal plasticity, have been proposed (Monnet and Mai, 2019). Earlier studies introduce micromechanical constitutive models in the framework of the theory of crystal plasticity, particularly for void growth and coalescence in irradiated fcc single crystals, and the evolution of irradiation damage loops during deformation (Barton et al., 2013; Ling et al., 2017; dong Lin et al., 2024). Ling et al. (2017) analyzed void growth and coalescence for irradiated fcc single crystals to assess and calibrate phenomenological models. Barton et al. (2013) have included the dislocation loops microstructure as a damage descriptor tensor to describe correctly the interactions between network dislocations and prismatic loops. Moreover, Barton et al. (2013) define a coupling between the evolution of damage descriptor tensor and shearing rate. The driving force for damage evolution is the shear strain rate. The nanovoid strengthening and the influences of void size on the material properties, such as stacking fault energies were investigated using Phase Field Dislocation Dynamics by Roach et al. (2023). The role of void swelling on plasticity and failure on neutron-irradiated stainless steel was analyzed by Vo et al. (2023).

This study employs atomistic simulations to predict the fundamental mechanisms governing the generation, evolution, and interaction of radiation-induced nano-defects under mechanical loads. Material deformation due to the evolution of radiation defects plays a pivotal role in material failure. The paper is organized as follows. To simulate the evolution of irradiation defects under mechanical loads, we prepare irradiated specimens where defects are generated through displacement cascades induced by highly energetic particles. In Section 2, we present the methods of point defects and more complex defect formation during the collision cascade in Fe–Ni–Cr alloy. To validate molecular dynamics simulations, we conduct an ion irradiation campaign with MeV energies. Section 3 provides Transmission Electron Microscopy (TEM) investigations that provide insights into structural changes resulting from ion beam irradiation and allow estimation of radiation-induced defect concentrations, which are compared with collision cascade simulation results. Section 4 is devoted to the deformation analysis of irradiated alloy during shear with different shear rates. Investigating the physical mechanisms of interaction between radiation-induced defects, their impact on the critical shear stress needed to activate blocked dislocations is discerned. In Section 5, the sequential interaction of dislocations with individual voids is analyzed. We identify a mechanism wherein dislocations cut through voids, leading to increased void density. Moreover, the simulations of dislocation-void interaction reveal that after the passage of several dislocations, a mechanism of void collapse and dislocation loop formation occurs, resulting in a coupling effect in the evolution of defects. This coupling effect between void collapse and dislocation loop formation implies a dynamic interplay between defects within the material. Based on the observed physical mechanisms a new irradiation hardening model is proposed in Section 6. The model incorporates the process of voids collapsing and considers the void size and distribution. The proposed model accounts for the coupling effect observed between void collapse and dislocation loop formation.

2. Preparation of the irradiated alloy

The atomistic behavior of FeNiCr samples was simulated using the MD method, and interatomic potentials based on the embedded atom model (EAM) were employed to depict atom-to-atom interactions (Bonny et al., 2013) with Ziegler-Biersack-Littmark (ZBL) corrections to account for short-range interactions. This task was performed using the Large-scale Atomic Molecular Massively Parallel Simulator (LAMMPS) (Thompson et al., 2022). Initially, a pure fcc Fe sample was generated with a lattice constant of 0.356 nm. Subsequently, Ni and Cr atoms were substituted for Fe atoms along $[\bar{1}01]$, $[1\bar{2}1]$, and [111] directions using the Atomsk numerical tool (Hirel, 2015) to create a $Fe_{55}Ni_{19}Cr_{26}$ alloy. Pristine samples were then produced through Monte Carlo simulations to obtain each potential metastable configuration at room temperature. Following this, the geometry optimization process aimed to reach the nearest local minimum of the energy structure. Additionally, the global force vector length of all atoms was kept less than or equal to 10^{-8} eV/Å. Subsequently, a 100 ps equilibration was conducted using an NPT thermostat at 300 K with a time constant of 100 fs (Dominguez-Gutierrez et al., 2022). This process continued until a uniform temperature and pressure profile were achieved, maintaining a density of approximately 8.0 g cm^{-3}.

Table 1
Size of the numerical boxes in nm as a function of the impact energy (PKA energy).

PKA (keV)	Num atoms	Atomic distribution	Box size [nm]
0.1–1	103 689	57 030 Fe; 26 959 Cr; 19 700 Ni	10.07_x; 10.47_y; 11.10_z
2–20	261 360	143 749 Fe; 67 953 Cr; 49 658 Ni	13.85_x; 14.39_y; 14.81_z
30–100	516 600	284 130 Fe; 134 316 Cr; 98 154 Ni	17.63_x; 17.88_y; 18.51_z

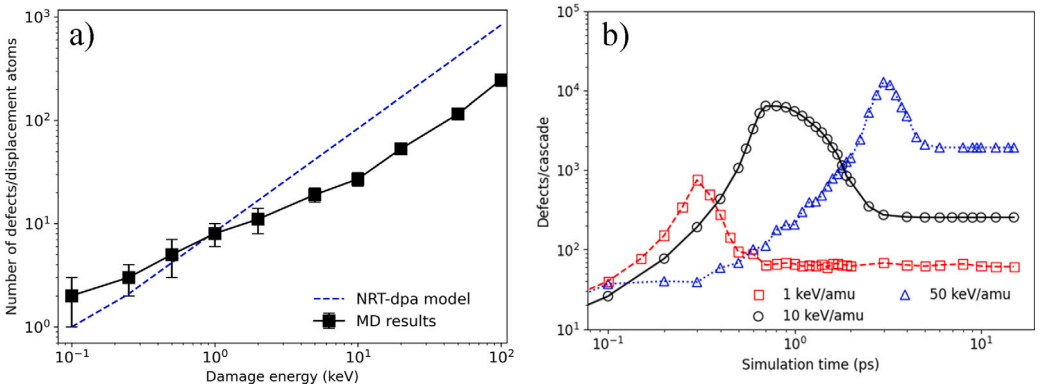

Fig. 1. The number of defects is shown as a function of the damage energy obtained by the CNA and Wigner method, in (a). The number of displaced atoms is plotted as a function of the simulation time for 1, 10, and 50 keV with a velocity vector parallel to the {111} plane, in (b).

2.1. Single collision cascades

To simulate radiation defects' production, we model the transfer of kinetic energy from high-energy particles to lattice atoms. This process results in the displacement of atoms, forming a primary knock-on atom (PKA) and initiating a collision cascade. The cascade typically includes a vacancy-rich core surrounded by a halo of self-interstitial atoms (SIAs). The displacement phase lasts about 10^{-11} s, followed by a thermalization process occurring after approximately 10^{-10} s. Experimental studies on single collision cascades are currently impractical due to rapid processes within the atomic lattice during irradiation. However, atomistic modeling using the MD method allows examination of the fundamental mechanisms of radiation-induced defect formation, elucidating irradiation damage in materials.

The numerical cell size for a single collision cascade should cover the entire trajectory of an implanted ion within the keV energy range, ensuring that the recoiling atom remains surrounded by lattice atoms within a larger cell (Nordlund et al., 2018a). Table 1 outlines the numerical box sizes used for each PKA value in this study. A single MD simulation is initiated by randomly selecting an Fe, Ni, or Cr atom located at the center volume of the numerical sample, and assigning kinetic energy (KE) in a range of 0.5–100 keV of PKA; during the ballistic phase and heat spike, to improve computational efficiency, a variable time step (0.00001-1.0 fs) was used, limiting atom displacements to a maximum of 0.02 Å per step. To mitigate cascade-induced shock waves, border cooling, and damping were implemented by applying a Nosé–Hoover thermostat on a 5 Å thick shell around the periodic borders of the cell. To demonstrate that radiation damage production is not dependent on stochastic anomalies, collision cascade simulations with 50 randomly directed energetic primary knock-on atoms (PKAs) are conducted for various PKA energies (1 keV, 2 keV, 5 keV, 10 keV, 15 keV, 25 keV, 30 keV, 50 keV, 100 keV).

The production of defects is analyzed as a function of PKA energy using common neighbor analysis implemented in the OVITO software (Stukowski, 2010), and is shown in Fig. 1(a). Cascades simulations include the threshold displacement energy (TDE) of 45 eV, which is the minimum recoil energy required to create a stable defect. Fig. 1(a) demonstrates that the number of replaced atoms increases linearly with damage energy following the Norgett, Robinson and Torrens (NRT) analytical model in a range of 0.1–20 keV, which is expressed as

$$N_d(T_d) = \begin{bmatrix} 0 & T_d < E_d \\ 1 & E_d < T_d < \frac{2E_d}{0.8} \\ \frac{0.8T_d}{2E_d} & \frac{2E_d}{0.8} < T_d < \infty \end{bmatrix} \tag{1}$$

The number of defects produced (N_d) by the damage energy (T_d) is determined by the threshold displacement energy (E_d), defined as the minimum recoil energy required to create a stable defect (Nordlund et al., 2018b). Fig. 1(b) illustrates the displacement atom profiles over simulation time for energy levels of 1 keV, 10 keV, and 50 keV. At 1 keV and 10 keV, the displacement atom profiles exhibit similar characters, but the dynamics differ significantly. Maximum values occur at different simulation times: 3×10^{-1} ps, 6×10^{1} ps, and 3×10^{0} ps for 1 keV, 10 keV, and 100 keV, respectively. The subsequent recombination process leads to the creation of stable point defects, with high-energy lattice atoms transferring kinetic energy to neighbors and displacing successive atoms from their lattice sites.

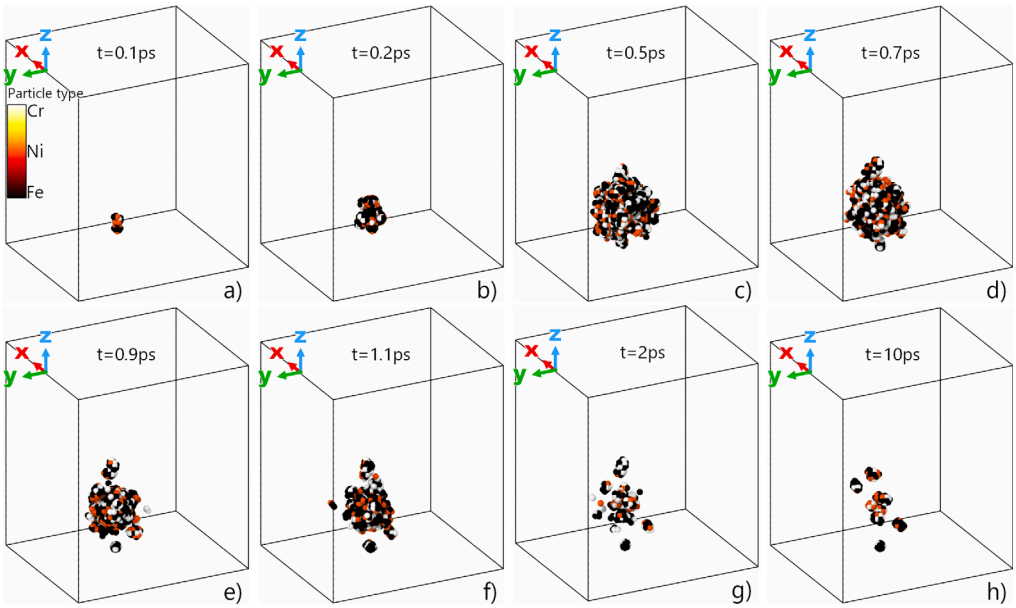

Fig. 2. Evolution of collision cascade in time induced by a 5 keV primary knock-on atom in NiFeCr alloy Number of defects as a function of the damage energy obtained by Common Neighbour Analysis, visualization of defects at different time step showing defects production.

In Fig. 2, the sequence of defect production during collision cascades at a PKA of 5 keV is presented. It is observed that the first defects are produced on the direction of the projectile velocity at 0.1 ps. The maximum defect production is observed between 0.4 to 0.7 ps. During the heat spike process, some atoms can reach supersonic speeds, transferring the kinetic energy of the projectile, resulting in the supersonic region in collision cascades simulations. After this point, the material undergoes a recovery process from 1 ps to 10 ps simulation time, and a recrystallization process occurs, where stable defects, known as Frenkel pairs, are formed during the thermalization process. The final point defects are presented in Fig. 2(h), where self-interstitial atoms and atoms located in the vicinity of single or bi-vacancies can be observed. The initiation of stable defects, specifically Frenkel defects, in irradiated crystalline solids occurs as the atomic collision process reaches thermal equilibrium with the system. This is followed by the recombination of displaced atoms with their original lattice positions. Frenkel pairs, a characteristic outcome of collision cascades, play a vital role in determining both the physical and mechanical effects, including those induced by stress application (Dominguez-Gutierrez, 2022; Nordlund et al., 2018a). The damage initiation process in the crystal structure involves the migration of point defects, such as vacancies and interstitials, which form defect clusters after the collisional phase of cascade evolution concludes. The range and distribution of damage in the material are influenced by the interaction of energetic ions with the material, resulting in coulombic losses of energy. The stopping power, dependent on various factors like the type of charged particle, kinetic energy, target material properties, and crystal orientation, determines the extent of damage. In our MD simulations, an electronic stopping correction is applied to account for the high PKA energy range, preventing overestimation of ion range. Obtained from SRIM with default values for the alloy, electronic stopping powers include inelastic energy loss from electronic collisions, applying a friction force to slow down fast-moving atoms.

2.2. Preparation of irradiated samples

The dpa value can be derived by utilizing the function of atomic displacement count (N_d) in relation to cascade energy, normalized with respect to the total number of material atoms N. Thus, the dpa parameter is determined by employing the damage energy (T_d), represented by the total ion energy (T_{PKA}). The expression for displacements per atom (dpa) is formulated as follows:

$$dpa = \frac{N_d(T_d)}{N} = \frac{1}{N}\frac{0.8(T_{PKA} - S_E)}{2E_d}$$

where T_{PKA} denotes PKA energy and S_E is the electronic stopping power correction. The energy loss to electronic interactions (S_E) is a retarding force due to interaction with matter.

To contain the heat spikes induced by 10 keV recoils (resulting in a dpa of 3.4×10^{-4}, as shown in Table 1), simulation cells were defined to avoid any influence from periodic boundary conditions on the outcomes. Temperature control during cascade simulations was limited to the sides of the cell, employing Langevin temperature control exclusively for the border atoms. Each collision cascade lasted 25 ps, ensuring no visible change in the damage structure of the cell and cooling down to 300 K. This approach resulted in a higher dose rate compared to experimental conditions. To ensure homogeneous irradiation, a randomly selected atom received

Table 2
The table summarizes the number of collision cascades calculated using Eq. (2) for various values of the dpa in the FeNiCr alloy by considering a PKA energy of 10 keV/amu.

dpa	0.02	0.12	0.14	0.31	0.57	1.32
Number of collisions	59	363	412	900	1500	3882

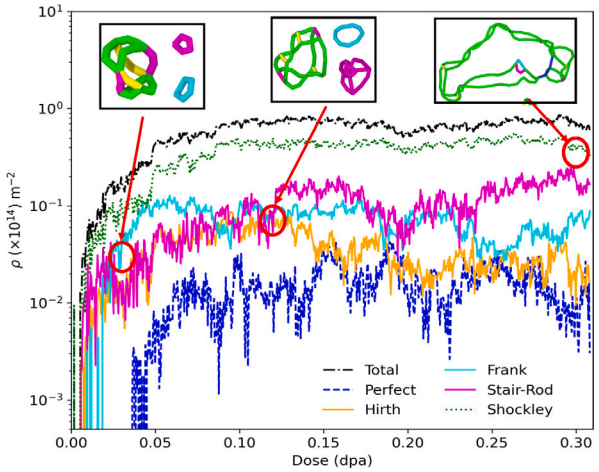

Fig. 3. (Color online) Dislocation nucleation and evolution as a function of irradiation dose. It is observed how dislocation loops nucleate and evolve with increasing irradiation dose (dpa) due to collision cascades. Initial stages involve Shockley loop formation, followed by increased Stair-rod density and Frank loop growth at intermediate stages. Later stages show Frank loops merging with or being absorbed by Shockley loops.

a velocity vector with a random orientation. An additional simulation step, including pressure relaxation to 0 GPa between recoil events, yielded identical results, within statistical fluctuations, to those obtained without the additional pressure control.

To subject the FeNiCr alloy to a dose of approximately 0.57 dpa, a total of 1500 consecutive simulations were performed. Throughout this overlap process, stress development was monitored (Dominguez-Gutierrez, 2022), revealing no significant buildup of stress. These findings align well with reported results for NiFe alloys (Granberg et al., 2016). Each set of 1500 recoils was repeated three times, utilizing different seed numbers in the random number generator and different initial random cells. This extensive approach aimed to demonstrate that the results were not influenced by stochastic anomalies. The specific value of dpa was determined based on the number of collision cascades, as presented in Table 2. The analysis of nucleated dislocations at various irradiation doses employed the Open Visualization Tool OVITO, utilizing its Dislocation Extraction Algorithm (DXA) (Stukowski, 2010, 2009).

In Fig. 3, we report results for the dislocation nucleation and evolution as a function of irradiation dose or number of overlapping collision cascades to follow the dynamics of dislocations up to 0.31 dpa, as the dislocation density stabilizes at higher dpa values. For the initial stages, collision cascades create self-interstitial atoms and single vacancies. These lead to the nucleation of small Shockley dislocation loops. These loops interact and further nucleate small Stair-rod and Frank type loops, as shown by the inset figure at a dose of 0.02. At intermediate stages, with continued overlap cascades, the density of Stair-rod dislocations increases being related to the formation of small stacking faults tetrahedra, while Frank type loops, once nucleated, tend to grow. Hirth dislocations are absorbed by Shockley loops, as highlighted a dose of 0.12. Later stages or higher doses, a small Frank dislocation loop positioned near a large Shockley partial chain can eventually join the chain. Frame-by-frame analysis reveals the entire structure converting into a complete Frank loop. We also observe the opposite phenomenon, where a large Shockley partial chain absorbs a Frank loop. This mechanism is in good agreement with reported phenomenology observed in FCC alloys (Levo et al., 2017).

Fig. 4 displays defect structures obtained from the DXA analysis, where differently colored lines represent various dislocation loop types, and blue semi-transparent surfaces depict voids and single vacancies. The dislocation and void densities for each analyzed sample are reported in Table 3. The total dislocation density, denoted as ρ_{Tot}, was calculated by dividing the total dislocation length, l_{Tot}, by the numerical cell volume V, while the void density was determined by dividing the number of voids without counting the number of single vacancies N_{void} by the numerical cell volume, V. During plastic deformation and irradiation hardening, it is crucial to identify various types of defects and understand the characteristics of the defect population, especially the distribution of defect sizes within the material. Changes occur in the size and quantity of voids and single vacancies during irradiation. For instance, the volume of single vacancies peaks at approximately 35 $\mathrm{Å}^3$, which remains consistent across irradiation levels as shown at the bottom panel of 4. It is noteworthy that the increase in vacancies with higher irradiation dose contributes to both small and larger void growth, as observed in the cumulative size distribution curve.

These three distributions demonstrate a similar trend, indicating a common pattern in defect growth across these states. The initial region (0–20 $\mathrm{Å}^3$) corresponds to the volume occupied by single vacancies and fractional spaces, influenced by both thermal

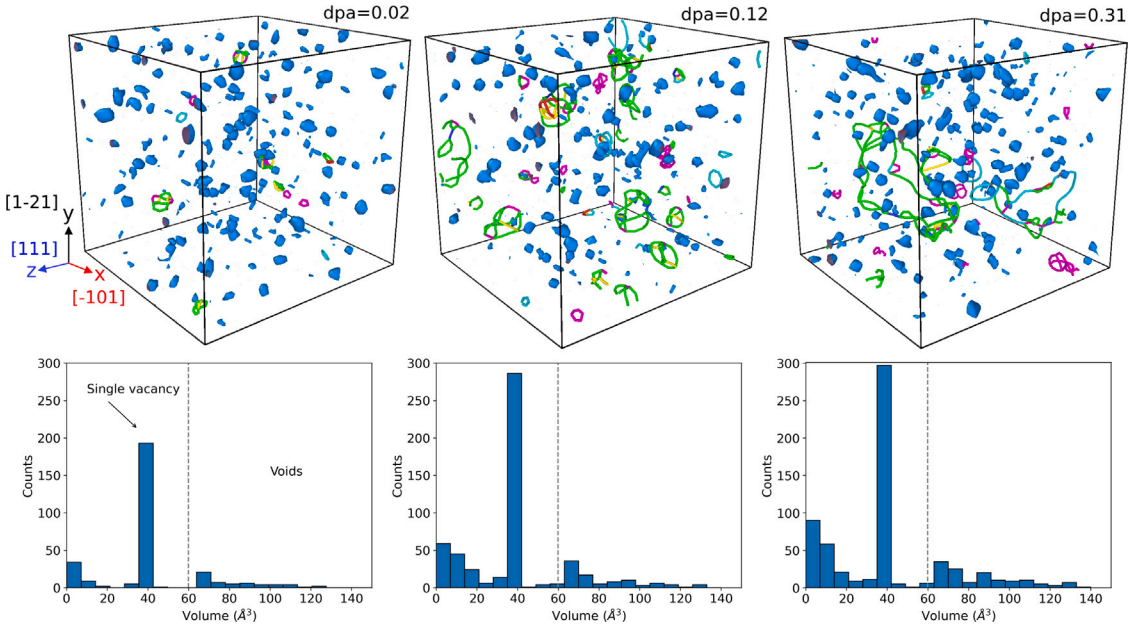

Fig. 4. The formation of dislocation loops and voids during the process is observed in a snapshot of overlap collision cascades at different irradiation doses for the FeNiCr at room temperature. Defect structures at different irradiation doses and corresponding to them the populations of radiation-induced voids and single vacancies. Production of single vacancies with a volume of ∼35 Å^3 is majority during the whole process. (For interpretation of the references to color in this figure legend, the reader is referred to the web version of this article.)

Table 3
Number of dislocation loops, length (nm), void volume (nm^3), and dislocation ($\times 10^{14}$ m^{-2}) and void densities (10^{25} m^{-3}) of irradiated sample at different dose.

Dose	Loop	Disc. length	Disc. density	Voids volume	Void density
0.02	11	38.31	1.28	4.95	1.91
0.12	26	227.78	7.63	8.45	3.38
0.31	13	174.22	5.84	12.33	4.69

motion and artifacts inherent in the tessellation method, followed by the second region (20–60 Å^3), representing the population of smaller voids. The third region (60–140 Å^3) anticipates the growth of larger void populations. The increasing void populations offer insights into the initiation and evolution of void clusters during irradiation, primarily driven by the absorption of surrounding irradiation-induced vacancies. Voids nucleate through the accumulation of large vacancy clusters and evolve by absorbing vacancies generated in subsequent collision cascades. Our simulations primarily unveiled the presence of Shockley partial chains and their corresponding clusters resembling HCP atoms, demonstrating slow growth and recombination upon nearing each other. In one scenario, a small Frank dislocation loop near a large Shockley partial chain merged with the chain, transforming into a complete Frank loop at a dpa of 0.31. Furthermore, we observed an instantaneous transformation of a Shockley partial chain into a Frank loop, a mechanism previously reported for FCC Ni-based solid solution alloys (Granberg et al., 2016).

3. Verification of irradiation effects by TEM observation

Ion irradiation has emerged as a valuable tool for the investigation of fundamental mechanisms underlying radiation damage in materials and the evaluation of material's radiation tolerance for diverse applications, including nuclear reactors and accelerator components (Skoczeń and Ustrzycka, 2016). The technique simulates the effects of radiation damage by subjecting materials to a high-energy ion beam, generating similar defect formations as neutron irradiation, such as point defects, dislocation loops, and voids (Nowak et al., 2023; Ustrzycka et al., 2020). By controlling the energy and fluence of the ion beam, various radiation conditions experienced by materials in nuclear reactors or space environments can be replicated. This method enables the rapid generation of significant damage levels without inducing radioactivity in the samples. In this study, a low carbon Cr-rich FeNiCr alloy is bombarded with an ion beam generated by a tandem accelerator using 1.5 MeV Ni (Nowak et al., 2023) with a fluence of 1×10^{15} ions/cm^2. The resulting radiation damage is 0.12 dpa (displacements per atom) and was calculated using SRIM (The Stopping and Range of Ions in Matter) software (Ziegler et al., 2010), to be into the range of the MD simulations. The ion-affected layers for Fe and Ni are approximately 0.8 μm, also determined through SRIM calculations.

Transmission electron microscopy (TEM) was used to study the microstructural evolution under irradiation. TEM investigations show the structural changes resulting from ion beam irradiation. In the studied material, direct observations of the defect

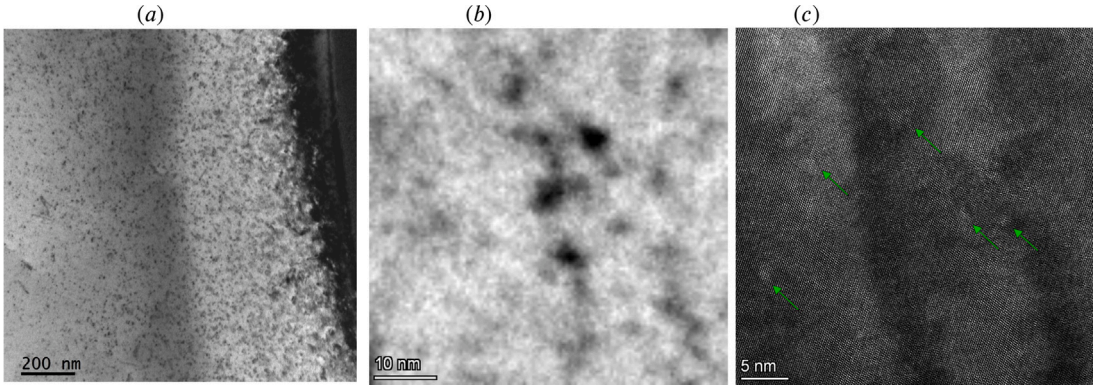

Fig. 5. TEM analysis reveals irradiation-induced defects in low carbon FeNiCr alloy at 0.12 dpa: (a) Defect clustering and (b) stacking fault tetrahedron formation due to irradiation. Visualization and identification of voids indicated by green arrows in (c).

structure, range, and radiation-induced defect concentrations were determined. Samples for TEM observations were prepared with a conventional lift-out method with the use of ThermoFisher Scientific Helios UX5 system. Gradually decreasing beam current was used for obtaining the electron transparency in the regions of interest. TEM observations were carried out with the use of JEOL JEM 1200 EX II operated at 120 kV for general observations and ThermoFisher Scientific Spectra 200 microscope (200 kV) for high-resolution observations of the radiation damage. Defects were quantified with line interception method previously used in similar studies (Chrominski et al., 2021; Wyszkowska et al., 2023).

Thin foil thickness was measured with Kossel–Moellestead convergent beam electron diffraction method (Williams and Carter, 2009). Fig. 5(a) displays the visualization of the irradiated region, revealing defect clustering. A magnified view is presented in Fig. 5(b), showing defects clustering and stacking fault tetrahedron (SFT) formation. Voids are identified in Fig. 5(c) with green arrows indicating their locations. The irradiation results in the formation of fine spot-like defects beneath the specimen surface, exhibiting relatively homogeneous distribution and an estimated size of approximately 1 nm. The total dislocation density is measured at 2.4×10^{14} m^{-2}, which is in good agreement with MD simulation results of 0.8×10^{14} m^{-2} at 0.12 dpa where the experimental value depends on the thickness of the lamela for TEM observations. MD simulations and experimental observations yield different results for void density due to inherent differences in their methodologies. This disparity is particularly notable in the assessment of total void density. In experimental measurements, only visible voids with a radius larger than 2 nm are typically considered, resulting in a total density of 1.0×10^{20} m^{-3}. In contrast, MD simulations account for small and large voids, leading to a higher density of 2.2×10^{25} m^{-3}. This discrepancy can be attributed to artifacts inherent to the MD method and limitations in the tessellation approach implemented in tools like OVITO and the utilized methodologies used in experiments and numerical simulations to quantify voids. Higher magnification images have been taken to reveal the interactions between previously established spot-like defects and new mobile dislocations. Fig. 6(a) provide an insight into these phenomena. It can be spotted that dislocation line cannot pass through the spot-like defect since it has been pinned. Higher magnification Fig. 6(b) shows directly that dislocation line encircles the round object and some segments of the line remain blocked. At the same time, the other parts of the dislocation line are susceptible to further glide. TEM analysis confirms the expectations the bowing dislocations are trapped in the potential produced by irradiation induced defects. These mechanisms are also observed in the MD simulations, accounting for the limitations inherent in the numerical method and the interatomic potentials employed.

4. Shear deformation of irradiated alloy

To comprehend the physical mechanisms contributing to irradiation-hardening in the mechanical deformation of simulation cells of irradiated alloys, an analysis was conducted. During shear deformation, the microstructure of irradiated material evolves due to the accumulation of internal strains, stresses, and radiation damage. The irradiation-induced defects undergo evolution and interact with other irradiation-induced defects as well as defects created due to plastic deformation. The irradiated samples employed in this study contain pre-existing defects, including voids and dislocation loops obtained during simulations of collision cascades (see Fig. 4). This approach allows for the analysis of the collective behavior of multiple dislocations interacting with numerous obstacles. Typically, MD simulations restrict the system to a singular dislocation and a few defects. Structural changes in irradiated samples up to 0.02 dpa during shear, with an imposed deformation rate of 0.2 Å/ps, are illustrated in Fig. 7.

In Fig. 7 (for $t = 0$), a schematic representation of the shear stress applied to simulation cells containing irradiated samples at various dpa levels is illustrated. The upper boundary experiences a constant shear loading along the $[\bar{1}01]$ plane at a rate of 0.2 and 1.0 Å/ps, choosing 0.2 Å/ps for this figure, while the bottom boundary remains fixed. Our boundary conditions allow for the construction of an infinite periodic glide plane for the edge dislocation along the x and y directions in the $(1\bar{2}1)$ plane. In the z–direction, we apply modified free boundary conditions, wherein atoms at the upper and lower surfaces are constrained to two-dimensional dynamics. A time step of 1 fs was employed for all simulations, conducted at room temperature (300 K), with temperature control maintained throughout the procedure. Atom positions and velocities were updated using the NVE ensemble.

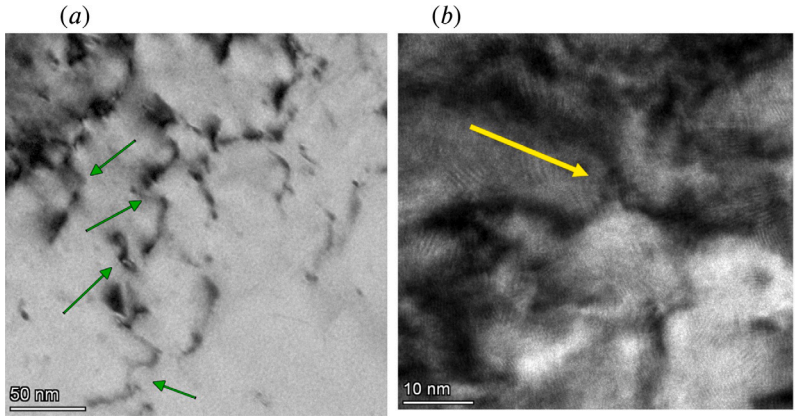

Fig. 6. Dislocation-blocking mechanism for the strengthening of FeNiCr alloy. (a) illustrates the presence of a dislocation line encircling a round object. (b) depicts a higher magnification, revealing that segments of the dislocation line remain blocked.

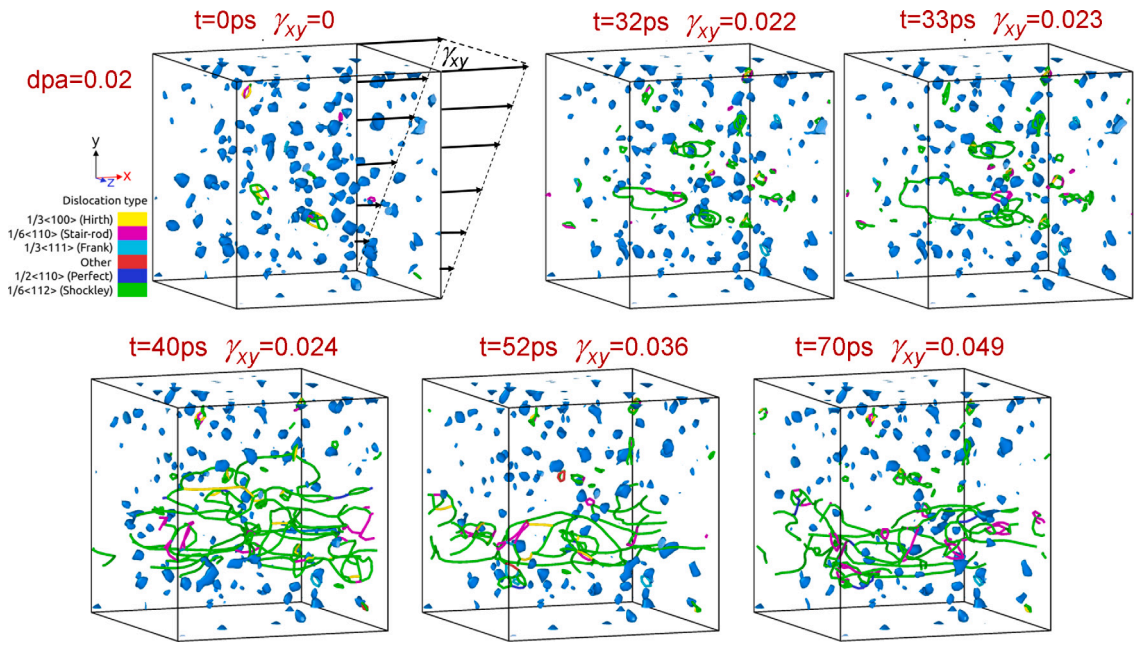

Fig. 7. Structural evolution of irradiated samples at 0.02 dpa during shear with a deformation rate 0.2 Å/ps.

Shear stress impacts the mobility of existing defects and plays a role in the creation of new ones. The behavior of irradiation-induced voids during shear deformation is intricate. The deformation of irradiated materials is governed by the stress-driven interaction of dislocations with radiation-induced defects. The population of voids evolves during shear deformation, and clusters of voids can undergo separation. The mechanism of voids collapsing into dislocation loops facilitates the accommodation of plastic deformation. Irradiation-induced voids and dislocation loops also act as pinning points for mobile dislocations. In the plastic regime, the interaction between dislocations and irradiation-induced dislocation loops becomes crucial. It is worth pointing out, that during shear deformation, expansion of dislocation loops is observed, their radius increase, structure rearrangement and increase of loop density (compare Fig. 7). Irradiation-induced loops act as sites for dislocation nucleation contributing to plastic flow. The dominant mechanism of plastic deformation is the well-known forest hardening mechanism. As the dislocation density increases, the movement of newly initiated dislocations encounters greater resistance within the pre- existing “forest” of dislocations. Consequently, forest hardening can be characterized as an elevation in the shear stress required to facilitate dislocation motion through the dislocation “forest”. The behavior of intersecting dislocations is elucidated by the formation of jogs (when dislocations intersect) or the formation of Lomer locks (when dislocations react with each other) (McElfresh et al., 2021). This mechanism exerts an influence on both the initial yield stress and the material’s hardening. However, in irradiated materials undergoing plastic shear localized plastic

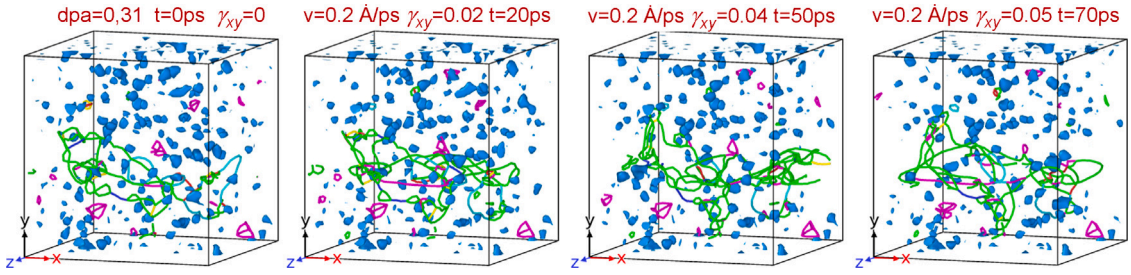

Fig. 8. Snapshot of shear-deformation simulation for irradiated samples to 0.31 dpa with rate 0.2 Å/ps.

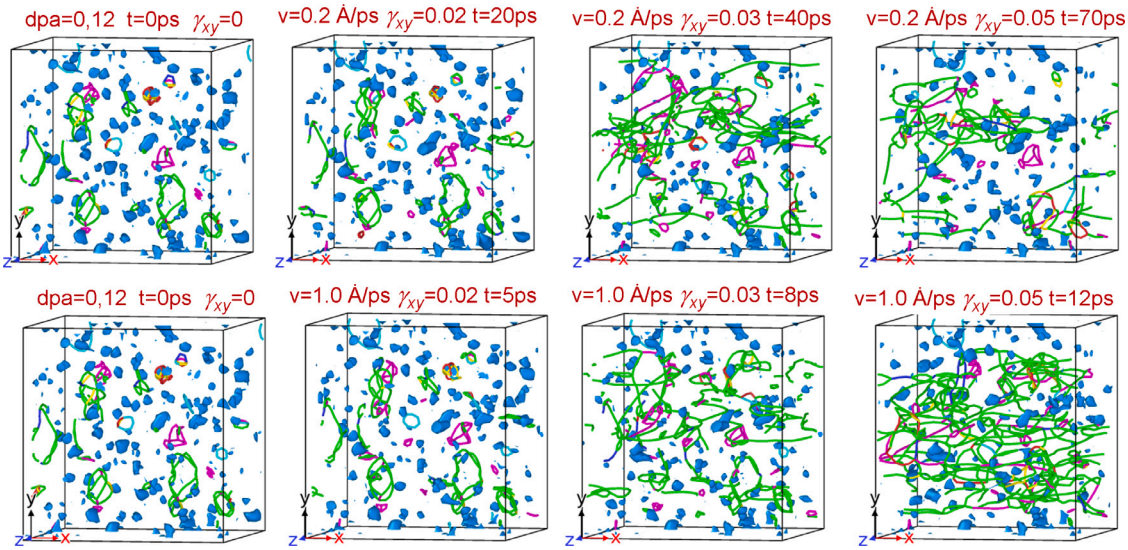

Fig. 9. Sequence of snapshots capturing shear deformation to 0.12 dpa with rates 0.2 and 1.0 Å/ps.

deformation is more likely to occur (see Fig. 7). In certain instances, dislocation lines can absorb dislocation loops, creating defect-free channels where plastic deformation localizes (further discussed in Section 6). Additionally, a higher initial dislocation density, particularly at elevated dpa levels, increases the likelihood of dislocations coming into proximity, resulting in annihilation events. High dislocation densities during equilibration stages, as depicted in Fig. 8 (t = 20 ps and t = 70 ps) and Fig. 9 (t = 40 ps and t = 70 ps), lead to more frequent annihilation events. As dpa and the initial number of dislocations increase, dislocation annihilation's become more prevalent during the equilibration stage (Fig. 9: v = 0.1, t = 20 ps and t = 70 ps).

The impact of different shear rates on the microstructure of irradiated materials is illustrated in Fig. 9, showcasing the structural deformation of the sample irradiated to 0.12 dpa at two shear rates 0.2 and 1.0 Å/ps. Higher shear rates generate more dislocations in less time, resulting in an increased dislocation density and accelerated damage accumulation. Conversely, lower shear rates limit the generation of dislocations, allowing them to move more slowly through the crystal lattice. Lower shear rates provide more time for material recovery, enhancing processes like defect recombination and leading to a gradual evolution of the microstructure. In Fig. 10, the results for the shear stress–strain curves at two different strain rates: 0.2 in (a) and 1.0 Å/ps in (b), corresponding to dpa values of 0.02, 0.12, and 0.31 are presented. The influence of pre-existing defects in the sample by comparing the results to those of the pristine sample is observed. It is evident that the yield point decreases as the defect density of the material increases, indicating a correlation between defect density and material yield behavior. The linear portion of the curves represents elastic deformation, whereas the oscillating region is associated with dislocations' initiation, movement, and annihilation. Different shear speeds lead to varying dislocation dynamics, influencing the evolution of shear stress. A decrease in the maximum shear stress value with increasing dpa dose, attributable to irradiation-induced defects is observed. However, in pristine conditions, the absence of pre-existing defects maintains the maximum value nearly constant across different strain rates, potentially serving as a reference for defect-free scenarios. While irradiation-induced defects can facilitate dislocation nucleation, they also impede dislocation motion as obstacles. As dislocations move through the crystal lattice, their movement can be impeded or even temporarily blocked by the presence of defects thus leading to irradiation hardening.

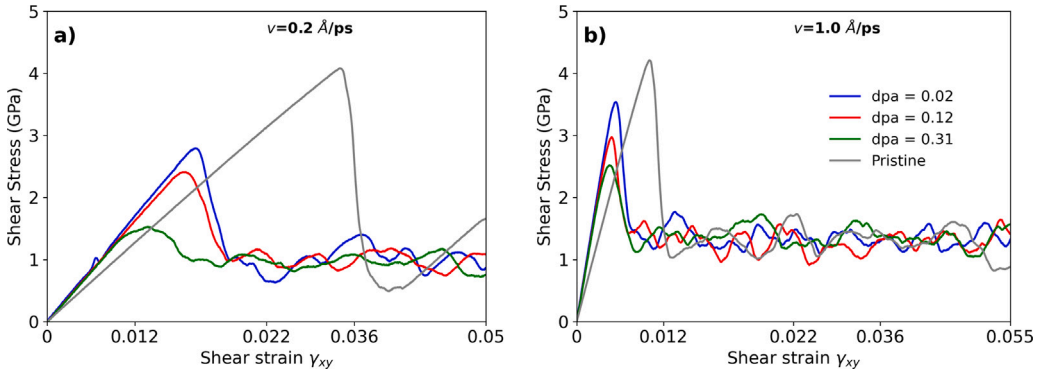

Fig. 10. Shear stress evolution with different shear rate for irradiated samples to different dpa levels, we include a comparison to the pristine case showing a decrease of the yield point due to the presence of irradiation-induced dislocations in the material.

Defect-free channels

Deformation localization revealed from the complex physical mechanisms responsible for plastic instability is widely observed in irradiated materials.

The mechanism of channel formation involves several stages. Initially, dislocations identify planes where they glide more easily, leading to the localization of plastic flow. As the process continues, dislocations interact with radiation-induced voids and loops. Cutting of voids by dislocations results in radiation hardening. This mechanism increases the density of voids while simultaneously reducing their size. If the voids become small enough, they collapse into dislocation loops. The interaction between radiation loops and dislocations results in loops absorption or annihilation, ultimately leading to a softening mechanism.

On the other hand, during the deformation of irradiated materials, dislocations are emitted from dislocation sources, which are typically situated at grain boundaries and inclusions. This process allows radiation-induced defects to also serve as potential sources for dislocation multiplication (compare Figs. 8 and 9). These dislocations travel along preferred glide planes through the matrix, encountering defect clusters like voids, dislocation loops and stacking fault tetrahedra (SFTs) in their trajectory. Moving dislocations interact leading to annihilation or absorption of radiation-induced defects. These processes are responsible for defect-free channel formation, deformation localization and softening behavior (Doyle et al., 2018; Ji et al., 2022). The phenomena of dislocation channel formation and strain localization are commonly observed in irradiation materials (Ding et al., 2016; Beck et al., 2017; Das et al., 2019). Experimental studies have shown that the reduction rate of radiation defects is much higher inside the dislocation channel, compared with that in the outside region (Ding et al., 2016). Therefore, the barrier effect induced by irradiation defects in this area is reduced quickly inside the dislocation channel. The formation of defect-free dislocation channels enhances plastic instability during deformation through localized plastic flow, also resulting in ductility reduction in other areas.

5. Identification of fundamental physical mechanisms responsible for the interaction of single radiation defects

The aim of this section is to present the fundamental physical mechanisms responsible for the interaction and evolution of individual radiation-induced defects, to model the impact of these defects on the material's mechanical behavior. Emphasis is placed on the significance of the physical mechanisms governing the interactions between dislocations and irradiation-induced defects to gain a comprehensive understanding of material behavior under coupled radiation and mechanical loads.

5.1. Formation of single defect: shear stress simulations

The study involved the construction of three models to investigate the physical mechanisms of interaction between irradiation-induced defects during mechanical loads.

Model I (Fig. 11,a), to comprehend the interaction mechanisms between Shockley dislocations and various voids during irradiation, shear stress simulations were conducted for an edge dislocation in the presence of a void. A simulation cell was constructed by introducing an edge dislocation and a void. The edge dislocation was created using the method proposed by Osetsky and Bacon (2003b), involving superimposing two crystals to form a periodic system. The model's dimensions were set to 27.86 $\mathrm{nm}_x \times 21.70\ \mathrm{nm}_y \times 20.36\ \mathrm{nm}_z$ to ensure an adequate size for applying shear stress loading and mitigating boundary condition issues. The simulation cell comprised approximately 1.0 million mobile atoms, and its principal directions aligned with $[\bar{1}01]$, $[1\bar{2}1]$, and $[111]$. Periodic boundary conditions were applied along the x and z directions, while fixed boundary conditions with a thickness of 0.5 nm were imposed in the upper and lower regions of the y direction with a $(1\bar{2}1)$ orientation. The study of the interaction and evolution of radiation defects at the atomic level in stainless steel utilized the FeNiCr interatomic potential based on EAM (Bonny et al., 2011, 2013). This potential accurately reproduced the stability of the fcc phase under large

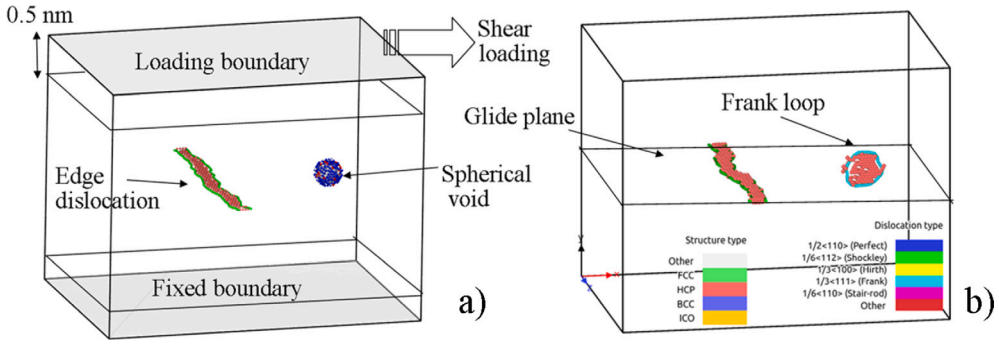

Fig. 11. Schematic of the simulation cells: (a) interaction of edge dislocation with radiation induced void (or precipitate) and (b) dislocation loop.

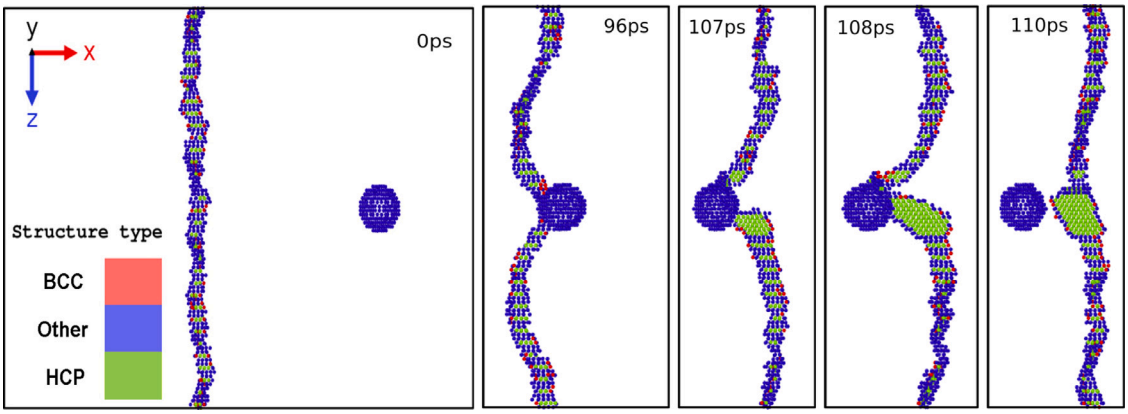

Fig. 12. Snapshots of the interaction between an edge dislocation and a void (with a diameter of 2 nm) are presented, illustrating the occurrence of the Friedel effect.

deformation, elastic constants, and stable stacking fault energy (SFE). The potential energy of the structure was minimized following the steps described in Section 2. During sample equilibration, a slight change in the lattice constant compared to the original value was observed. Subsequently, the perfect dislocation in **model I** was dissociated into two dislocations, initiating shearing by displacing the upper grip in the simulation box.

Model II (Fig. 11,b), the simulation cell in this case followed the same construction procedure as the second model, with a specific focus on studying the interaction between a Shockley dislocation and a Frank loop a common mechanism observed during irradiation. The insertion of a dislocation loop was accomplished using the method outlined by Baudouin et al. (2015). The Frank loop was constructed based on the Thompson tetrahedron notation, where four {111} planes were built, and the loop could adopt one of these proposed planes. The formation of the $1/3\langle 111\rangle$ loop occurred after system relaxation, positioning its center within the dislocation glide plane. This ensured stable dislocation glide and the stability of Frank loops at room temperature, a crucial aspect for atomic-level plasticity studies. The introduction of the dislocation loop took place after constructing the edge dislocation within the simulation box. Each configuration was characterized by the native plane of the Frank loop.

5.2. Exploring the mechanisms of dislocation-void interactions

Significant effects on the mechanical properties of irradiated material are observed due to the interactions between radiation-induced voids and linear defects in the crystal lattice. Voids, resulting from the aggregation and coalescence of vacancies, are typical radiation defects where large voids are formed as point defects, such as vacancies and interstitials, migrate and coalesce within the material due to diffusion. The presence of radiation-induced voids in the material leads to among others irradiation swelling, causing dimensional changes and deformations. Thus, the consequences of voids in the material are significant and adverse to its properties. Consequently, the interaction processes between empty space and edge dislocations have been examined, and the corresponding interaction mechanisms were analyzed using MD simulations. Our study focuses on typical radiation-induced defects in the form of spherical voids with diameters ranging from 1 to 5 nm, which can be compared with TEM results (see Fig. 5).

It is well known that when a dislocation encounters a barrier, it has two possibilities: cutting through the barrier (known as the Friedel effect) or bending around the void until it is completely enclosed, creating a dislocation loop through the Orowan

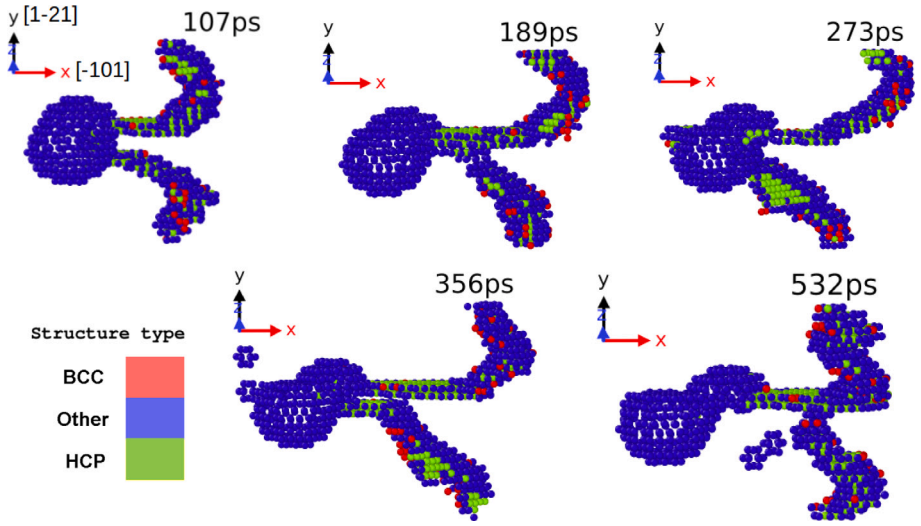

Fig. 13. The mechanism of void cutting by dislocation at different time steps, demonstrating the cut of the spherical void by the two partial dislocations during shear stress, is revealed through MD results.

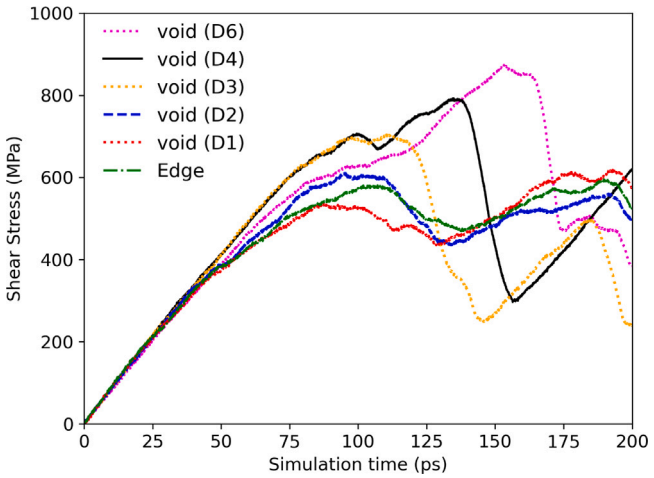

Fig. 14. Shear stress evolution in a Fe–Ni–Cr alloy during the interaction of an edge dislocation with voids of different sizes. D*N* denotes a void diameter of N nm. Results for the case without a void are included as a reference.

mechanism. Radiation-induced voids are not transparent to dislocation motion, in this case, the cutting mechanism is observed. The mechanisms accompanying the interaction of an edge dislocation with a void were identified employing MD simulations. Snapshots of the interaction between a dislocation and a void showing the Friedel effect are presented in Fig. 12. Under the applied force, the split dislocation moves and approaches the void. When a dislocation line encounters the void, regardless of the characteristics of the matrix, it bows. The dislocation segment that is pinned to the void resists further glide (Fig. 12: (96 ps)). As the deformation continues to increase, the dislocation bows (Fig. 12: (107 ps, 108 ps)) until it breaks away at the critical shear stress (Fig. 12: (110 ps)).

The mechanism of unpinning the dislocation occurs due to the application of external stress and involves the re-arrangement of the dislocation within the crystal lattice structure. This allows the dislocation to continue moving. It was observed that the mechanism causing the resistance formation in the void changes as the radius increases. Radiation-induced voids are characterized by surface tension that results from cohesive forces between atoms on the surface. Surface tension affects their growth and interaction with dislocations and other defects. The presence of voids generates stress fields that attract dislocations but at the same time impede their movement.

Despite this, the movement of dislocation can cause deformation of the void, as observed in the Friedel effect (Fig. 13). The mechanism of cutting a void by a dislocation involves the interaction between the atoms at the void's edge and the dislocation. As the dislocation advances, it induces a separation of the atoms at the void's edge, leading to a displacement of a portion of the void (Fig. 13). The upper section of the void (on the compressive side of the dislocation) becomes displaced relative to the slip

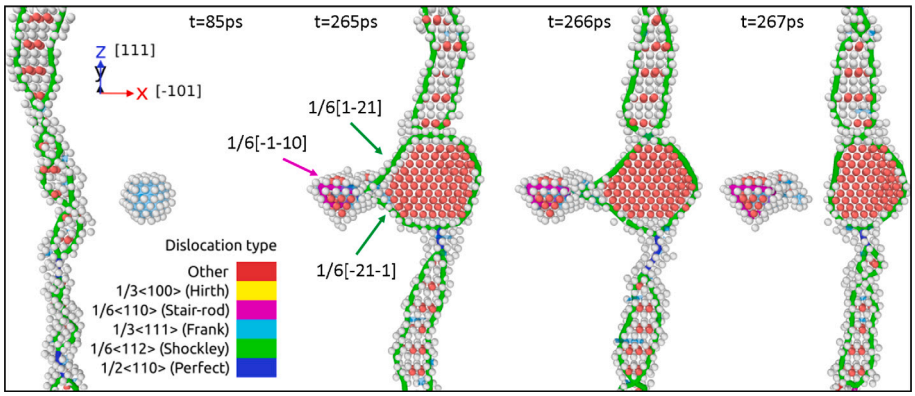

Fig. 15. Mechanism of void (D1) collapse after the passage of edge dislocations, resulting in the formation of an SFT mainly formed by stair-rod dislocation in agreement with the Silcox–Hirsch mechanism.

plane of the dislocation, with a displacement corresponding to the Burgers vector. The size and shape of the displaced structure are determined by the void size, dislocation velocity, and dislocation energy (Marian et al., 2005; Liu, 2015). Additionally, as the dislocation moves through the void, it prompts atomic rearrangement, potentially resulting in the formation of new crystal structures or the generation of new defects or voids within the material (Fig. 13: 356 ps and 532 ps). It is worth noting here that, the mechanism of voids cutting leads to an increase of voids density defined by the number of voids N_{void} divided by V. Voids divided into smaller ones become additional barriers to dislocation movement and thus contribute to an increase in irradiation hardening. Moreover, it is believed that the mechanism of voids cutting by dislocations, leading to the collapse of voids into loops, which then can annihilate during interaction with the dislocation, is responsible for the formation of the dislocation channel and the localization of plastic flow (Hatano and Matsui, 2005). Complex stress histories are generated by the interaction of void (diameter D between 1 and 6 nm) with dislocations under constant deformation rate of 0.03 Å/ps in a crystalline material. The shear stress history corresponding to the mechanisms of dislocation pinning and unpinning from the void is presented in Fig. 14. The presence of the void impedes the dislocation's motion, restricting its ability to glide through the lattice. The unpinning mechanism enables the release of a dislocation from its trapped or immobilized state, allowing it to resume its motion through the crystal lattice. In addition, the highest stress refers to the critical stress required to unpin the dislocation from the void. The value of this critical stress strongly depends on the size of the void. Larger voids necessitate higher stress levels to facilitate dislocation release, as illustrated in Fig. 14. It is noteworthy that we observed no reduction in stress curve despite the varied void sizes, indicating the persistence of high stress levels across the samples. In Fig. 15 we present the visualization of the interaction between the edge dislocation and the void, showcasing a phenomenon known as void collapse nucleating a stacking fault tetrahedron, as described by the Silcox–Hirsch mechanism. This mechanism involves the reaction of Shockley partials at each intersection of {111} planes, resulting in the formation of stair-rod partial dislocations (Wirth et al., 2000). An example includes $\frac{1}{6}[1-21]+\frac{1}{6}[-21-1]=\frac{1}{6}[-1-10]$, along with other symmetrical cases. The presence of these dislocations is characterized by the existence of one or more additional half-planes of atoms within the crystal lattice structure, leading to a jog dislocation or a kink dislocation. The creation of dislocation loops can be attributed to the minimization of elastic energy within the material and the accommodation of excess strain energy, resulting in a localized distortion in the lattice. These results indicate that the size of the void is important in determining the critical stress required to unpin the dislocation. Finally, the process of interaction of the void with the forest of dislocations can lead to collapsing of the void and forming a dislocation loop.

However, compared to the description of the mechanisms of void growth and coalescence, only a small number of works are devoted to the mechanism of collapse of the nanoscale voids (Galitskiy et al., 2023; Guan et al., 2019; Tang et al., 2018; Xiang et al., 2017; Peng et al., 2016; Li et al., 2014; Davila et al., 2005). In recent years, Xiang et al. (2017) have revealed two mechanisms of void collapse: the plasticity mechanism and the internal jetting mechanism. Tang et al. (2018) pointed out that the collapse of voids is facilitated, as the specific surface area or impact velocity increases. Peng et al. (2016) analyzed the process of void collapse under loading and void re-nucleation and coalescence under unloading conditions. Small voids, similar in size to radiation voids, were analyzed. Peng et al. (2016) examined the anisotropy of void coalescence under loading and unloading conditions using different impact directions. As a result of the conducted analyses, the voids collapsed after the shock loading, leaving two disordered regions at the initial voids sites. But, voids re-nucleated in these disordered regions and grew by the emission of dislocations. Guan et al. (2019, 2021) show, that the collapse of void is mainly due to the emission and growth of the dislocations under high strain rate loading. Therefore, the deeper reason of the void collapse is the intrusion of the disordered atoms on the void surface.

5.3. Interaction between dislocation and dislocation loop

The exploration of interactions between dislocations and Frank loops has been conducted through MD simulations by Osetsky and Bacon (2003b), Baudouin et al. (2015), Rodney (2004), and Cui et al. (2017). The interaction of dislocations with Frank loops has

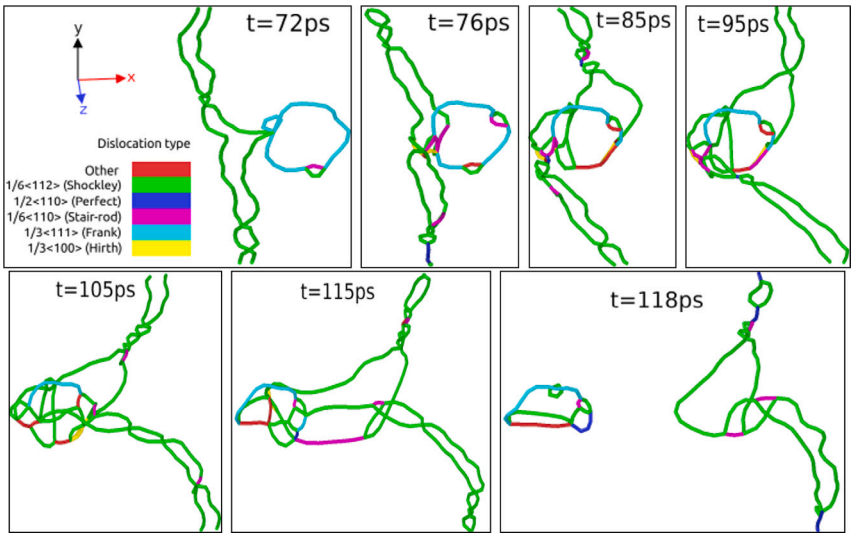

Fig. 16. Snapshots of edge dislocation interacting with Frank loop (D = 3 nm).

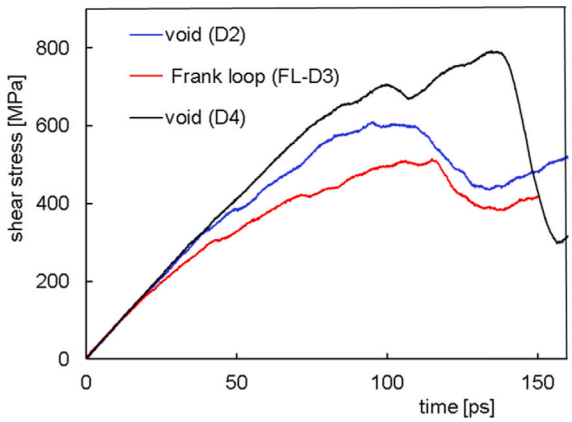

Fig. 17. Shear stress evolution during the interaction of dislocation with voids (D2 and D4) and interaction of dislocation with Frank loop (FL-D3) (where D N denotes the defect diameter of N nm).

been identified by Baudouin et al. (2015) as a crucial process in the formation of channels, leading to localized plastic deformation in irradiated materials.

In this section, the interaction between an edge dislocation and an interstitial Frank loop in a Cr–rich FeNiCr model system is investigated. The main focus is to understand the underlying physical mechanisms of their interaction and to determine the critical stress required for the dislocation to become unpinned. The methodology proposed by Rodney (2004) for constructing the Frank loop in a face-centered cubic (FCC) crystal is employed (see Fig. 11(c)). To initiate the simulation, a set of interstitial atoms forming the Frank loop is inserted between two (111) planes in the simulation cell. Prior to the shear simulations, an energy minimization is conducted without applying any external stress. This allows for the dissociation of the edge dislocation in its glide plane and the relaxation of the Frank loop (D = 3 nm) located on the glide plane of the Shockley partials, preparing it for subsequent shear simulations at room temperature. When the dislocation approaches the Frank loop, there is an interaction between the stress fields around the dislocation and the loop. This interaction causes the Frank loop to split into smaller loops and transform into a different type of dislocation loop. Eventually, a significant portion of the Frank loop is absorbed by the dislocation. Throughout this interaction, both the dislocation line and the Frank loop undergo deformation. The dislocation line bows and bends around the loop, adjusting its shape to accommodate the presence of the loop.

As presented in Fig. 16, the first mechanism is pinning and unpinning, where the presence of the Frank loop creates a local stress field that interacts with the approaching dislocation hindering the dislocation from easily passing through or bypassing the loop. The second mechanism is loop shearing, which involves the movement and deformation of the loop caused by the interaction with the dislocation. The third mechanism is loop unfaulting, as identified by Baudouin et al. (2015) and Cui et al. (2017). Loop unfaulting converts the interstitial loop into a perfect loop, resulting in a different configuration. The fourth mechanism is loop

absorption, which occurs when a dislocation line absorbs or incorporates a dislocation loop into its structure. These mechanisms collectively explain the complex interactions observed between the edge dislocation and the Frank loop. The shear stress evolution during the interaction of dislocation with voids (D2 and D4) and with Frank loop (FL-D3) is shown in Fig. 17. The obstacle strength parameter is different for different obstacles and numerous estimations (Osetsky, 2021) always demonstrate that the dislocation loop strengthening parameter is about 3 times weaker than that of voids. Moreover, atomistic estimation of dislocation loop and void strengthening effects indicates that nanometric voids are much stronger obstacles than dislocation loops of comparable size. Thus, loops smaller than 5 nm were found to be weaker obstacles than even 2 nm voids. Even the higher concentration of small dislocation loops cannot compensate for their weak resistance to dislocation motion. It is, therefore, obvious that radiation-induced strengthening due to voids cannot be ignored when estimating material mechanical property changes.

6. Irradiation hardening model

The establishment of constitutive equations based on the physical mechanisms governing the evolution of microstructure features is necessary to predict the radiation effects on mechanical properties. The interaction of irradiation-induced defects with structure defects directly controls the collective mechanical response of the material. Radiation-induced defects impede the movement of dislocations, resulting in irradiation hardening (Osetsky, 2021; Osetsky and Bacon, 2010; Rodney et al., 2001). On the other hand, these defects can be displaced, absorbed or broken by dislocations, thereby creating defect-free channels (Ji et al., 2022, 2023). Dislocation barriers also contribute to increased material embrittlement resulting from plastic flow localization. In the literature, materials with a high concentration of barriers are characterized by a continuous field of barriers represented by two key factors: the density and size of the barriers (Kocks and Mecking, 2003). Continuum equations are based on these two variables and their evolution is formulated as a function of the degree of plastic deformation. Generally, the hardening law for irradiated material formulated within the continuum mechanics is based on three terms containing the density of dislocations, density of dislocation loops and additional phenomenological terms proposed to account for a dislocation unlock mechanism (Barton et al., 2013; Hure et al., 2017; Ling et al., 2017). Although radiation-induced strengthening due to voids is stronger than strengthening due to dislocation loops, voids were not taken into account. Typically, irradiation hardening is incorporated as additional components in a linear manner into the mechanical response of materials. This approach leads to the independence of these terms from the initial yield strength.

The main objective of this section of the article is to describe the hardening effect of such barriers and formulation of kinetics laws of barrier-dislocation interactions. This concept aims to introduce deformation mechanisms, physical mechanisms that these defects undergo to the constitutive relations. A series of theoretical models have been developed in the literature to characterize the critical resolved shear stress (CRSS) for dislocation bypassing defects. They can be categorized into two kinds: the cascade-induced source hardening (CISH) model (Bao et al., 2023) and the Orowan-type hardening model. For strong obstacles (like precipitates or clusters of dislocation loops), unpinning the dislocation occurs through the Orowan mechanism, under heightened stress, the dislocation bends around the defect, creating an Orowan loop (Tsugawa et al., 2022). The Bacon–Kocks–Scattergood (BKS) model is the typical Orowan-type hardening model (Lehtinen et al., 2016; Wu et al., 2022; Liu et al., 2023; Xu et al., 2019). Bacon et al. (1973) have developed the BKS model to describe irradiation hardening for strong irradiation defects. Moreover, the modified BKS model is also widely used to describe the hardening effect induced by sheared voids (Xu et al., 2019; Ji et al., 2022). In the case of the sheared void, the array of dislocations bypassing it gradually weakens the void until it divides the initially spherical void into two parts. Yu et al. (2022) proposed that the hardening effects of sheared voids can be quantified by a modified Bacon–Kocks–Scttergood model if adopting an effective diameter that is calculated from the major axis of the dislocation-void intersection region rather than the constant diameter of the unsheared void. Modified BKS model based on the average value of voids distance L_v and the comprehensive characteristic length for hardening L_H is expressed in the following form

$$\tau_H^v = \frac{\mu b}{2\pi L_v}\left[ln\left(\frac{L_H}{r_c}\right) + \Delta\right] \tag{2}$$

where τ_H^v denotes the necessary hardening stress to unpin a blocked dislocation on a void to restart it, r_c is the radii of the dislocation core (following Bacon et al., 1973, $r_c = b$, b is Burgers vector magnitude). Δ is a fitting parameter, depending on the interaction between dislocation and matrix-obstacle interface and is related to surface energy in the case of voids (Yu et al., 2022). Liu et al. (2023) showed that the optimized value of Δ parameter to -0.573 fit the DD data in tungsten (bcc). Yu et al. (2022) proposed the fitted BKS model with $\Delta = -0.006$. Δ is suggested by Bao et al. (2023) to be 0.7 for precipitates and 1.52 for radiation-induced voids in bcc Fe. In the proposed model, the value of the Δ parameter is adopted after (Bao et al., 2023), even though this value may not be directly compatible with the fcc structure. The surface energy of voids depends on the type of structure (bcc or fcc) of the material because the surface energy is influenced by the packing densities and arrangement of atoms on the surface of the void. However, the literature data do not clearly specify the value of the Δ parameter for Cr-rich alloys with fcc structure.

The comprehensive characteristic length for hardening L_H is defined as the norm of void characteristic length L_v^{eff} and dislocation characteristic length L_D with $n = 1/2$ (Ji et al., 2022, 2023), in the following form

$$\left(L_H\right)^{-n} = \left(L_v^{eff}\right)^{-n} + \left(L_D\right)^{-n} \tag{3}$$

where the two characteristic parameters for radiation void: diameter D_v and spacing L_v are integrated (compare Ji et al., 2023) into one effective characteristic length of a void as

$$L_v^{eff} = \frac{L_v D_v}{L_v + D_v} \tag{4}$$

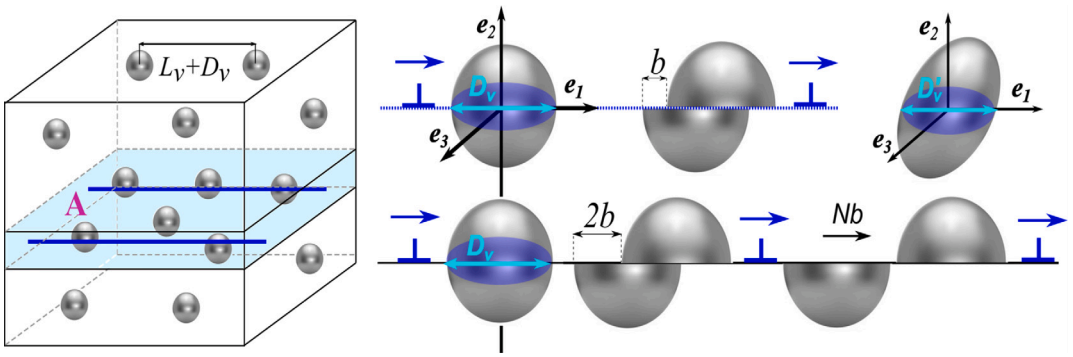

Fig. 18. Void cutting model.

BKS model can be also expressed by the hardening coefficient α_{BKS} (Bao et al., 2023) reflecting the pinning strength of the barriers

$$\tau_H^v = \left[\frac{1}{2\pi}\left(ln\left(\frac{L_H}{b}\right)+\Delta\right)\right]\frac{\mu b}{L_v} = \alpha_{BKS}\frac{\mu b}{L_v} \tag{5}$$

where $\frac{\mu b}{L_v}$ is a classical value of Orowan bowing.

Based on the physical mechanisms responsible for the interaction of radiation defects with lattice defects identified in Section 5, a mathematical description of the phenomena underlying radiation hardening is formulated. The proposed model is based on three phenomena: mechanism of void cutting (mechanism related to the decrease in the diameter of the void and, consequently, to its splitting); mechanism of void shrink as a result of absorbing the outermost vacancies and mechanism of void collapse (mechanism of small voids transformation into dislocation loop). In this section, each part of the model will be derived separately. The proposed model aims to develop phenomenological approaches to more physics-based formulation. Although Cr-rich alloys are analyzed here, the model can easily be extended to other materials.

6.1. Void deformation

Atomistic simulations make it possible to reveal the physical mechanisms of the interaction of the void with the dislocation and behavior of radiation defects after shear. Based on the analysis in Section 5, the distinctive quantities to characterize the hardening stress can be identified including the void diameter D_v and spacing L_v, and the distance Nb over which the upper part of the void is displaced after the passage of several dislocations. Radiation-induced nano-voids are cut by dislocations (compare Fig. 13), two parts divided by the slip plane, are shifted relative to each other by one Burgers vector each time the dislocation interacts with the void. Thus, the shape of the void changes from spherical to ellipsoidal and the diameter of the void also changes. If the dislocation density is sufficient, the cutting mechanism can lead to the division of larger voids into smaller ones, increasing the voids number (compare Hatano and Matsui (2005), Landeiro Dos Reis et al. (2018) and Yu et al. (2022)).

Void cutting model

The mechanism of cutting the void is shown in Fig. 18. During the interaction of the edge dislocation with voids, dislocation interacts with the void boundary and as a result, the top and bottom of the void are shifted relative to each other by one Burgers vector b. The passage of N edge dislocations results in the displacement of the upper part of the void by Nb (Fig. 18). One dominant slip system resulting in the largest part of the deformation is considered, thereby establishing the upper limit of the change. The assumption of the homogeneous distribution of voids of the same size and the constant volume of the void during deformation is adopted (Fig. 18).

Kinetic model of voids

The void cutting model allows deformation of the void by changing its diameter ($D_v \rightarrow D'_v$) after the passage of several dislocations (Nb). In the course of a deformation process, the initially spherical void transforms to a flattened elliptical shape. Therefore, assuming that the volume of the void does not change, deformation occurs by changing its diameter. The current value of void diameter takes the form

$$D'_v = \begin{cases} D_v - bN & \text{for} \quad bN < D_v \\ 0 & \text{for} \quad bN \geq D_v \end{cases} \tag{6}$$

The single step formed due to the displacement of the upper part of the void relative to the lower part corresponds to the Burgers vector b. Iterating this procedure for N times is equivalent to the passage of N edge dislocations. However, when bN exceeds or is

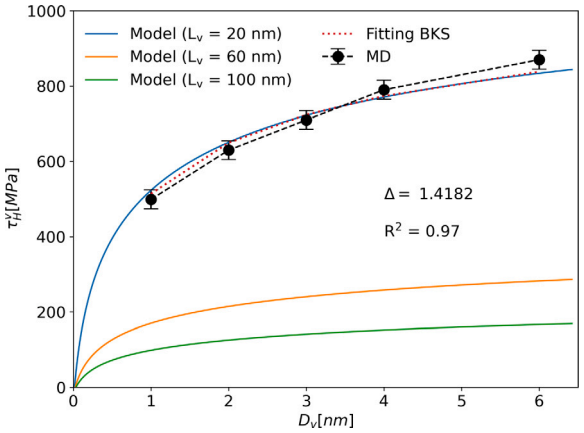

Fig. 19. The modified BKS model (solid lines) is calibrated based on MD simulations (dashed red line) to predict the decrease in shear stress with increasing void diameter (D_N) due to void cutting. The Δ-parameter was extracted through fitting the model to MD simulation data. (For interpretation of the references to color in this figure legend, the reader is referred to the web version of this article.)

equal to the void diameter ($bN < D_v$), D' is set to zero. This additional condition ensures that the current value of void diameter D'_v does not become negative and reflects the physical behavior of voids, where the original void splits into two new ones. This condition also becomes a criterion for dividing a single empty space into two smaller ones. As a result of splitting a single void of diameter D_v, the initial density of the voids N_v defined as a voids number per unit volume increases due to the increase in the number of voids.

The reduction of void diameter is equivalent to the expression

$$\Delta D_v = \begin{cases} -bN & \text{for} \quad bN < D_v \\ 0 & \text{for} \quad bN \geq D_v \end{cases} \tag{7}$$

Using the Orowan equation relating to the mobile dislocation density ρ_{D_v} the above equation (for $bN < D_v$) can be expressed by the shear strain rate $\dot{\gamma}^p$ in the following form

$$\Delta D_v = -\frac{N}{\rho_{D_v} \Delta x} \Delta \gamma^p \tag{8}$$

where Δx denotes the distance covered by the moving dislocations. The evolution of the hardening stress τ_H^v necessary to unpin a blocked dislocation on a void with decreasing diameter due to the mechanism of void cutting is shown in Fig. 19. The modified BKS model was calibrated based on the results of multiple MD simulations to extract through fitting the values of the Δ parameter to ensure the model will output data that are close to actual data. The hardening stress was determined from the Eqs. (2)–(8). Δ was found to be 1.4182 for fcc Fe–Ni–Cr Alloy. The high correlation coefficient ($R^2 = 0.97$) demonstrates the accuracy of the fitted BKS model in predicting the MD simulation results.

Fig. 19 shows the fitting BKS model and the MD obtained CRSS (based on the results shown in Fig. 14) for different voids distance L_v. The values of the L_v parameter defining the voids distance were adopted consistent with the void distances defined in the MD simulations by the numerical cell size (≃20 nm) and periodic boundary conditions. As expected, CRSS increases with void diameter and is higher for densely packed voids (for lower L_v values). As the void diameter decreases due to shear mechanisms, the stress needed to overcome the pinning effect also decreases. This is because the smaller voids offer less resistance to dislocation movement compared to larger voids. Eqs. (2)–(8) capture the specifics of the interaction between dislocations and voids, and the dependence of the hardening stress on void spacing.

The effects of the dislocation glide plane distance from the void center on the void deformation

The stress increase resulting from the Friedel effect that occurs when a void is traversed by a dislocation is analyzed. The localized stress field around the void, induced by the dislocation-void interaction leads to the pinning of the dislocation and an increase material hardening. The cutting effect involves the displacement of the upper part of the void with respect to the dislocation slip plane by the Burgers vector length. This displacement increases the boundary area and raises the critical shear stress. In this section, the influence of the distance between the dislocation glide plane and the void center on void deformation is examined (Fig. 20). The situation where a dislocation penetrates the void center is a special case because the relative position of a void to a glide plane is arbitrary. This distance directly influences the stress field and the interaction between dislocation. In this subsection, the effect of the position of the displacement slip plane relative to the center of the spherical void on the critical shear stress is analyzed. MD simulations show that the asymmetry of the critical shear stress occurs depending on the position of the glide plane relative to the void. For the slip plane located at the top or bottom of the void, the critical shear stress is not equal even if the impact parameter d from the void center is the same (compare Fig. 20(a) and (b)). The impact parameter $d = 2D_{vp}/D_v$ is defined by the distance from

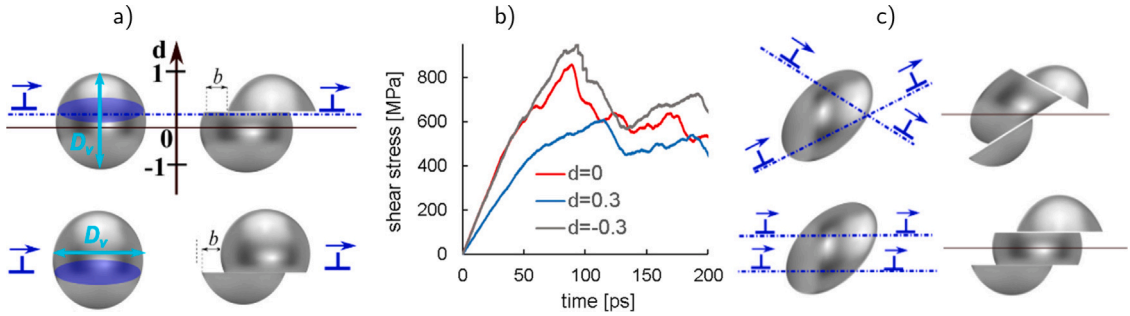

Fig. 20. Model illustrating the asymmetrical effect of distance between the void center and a glide plane on the pinning strength; (a) definition of impact parameter d; (b) shear stress evolution (from MD results) for different impact parameter d; (c) arrays of slip planes for dislocations motion during the interaction with void.

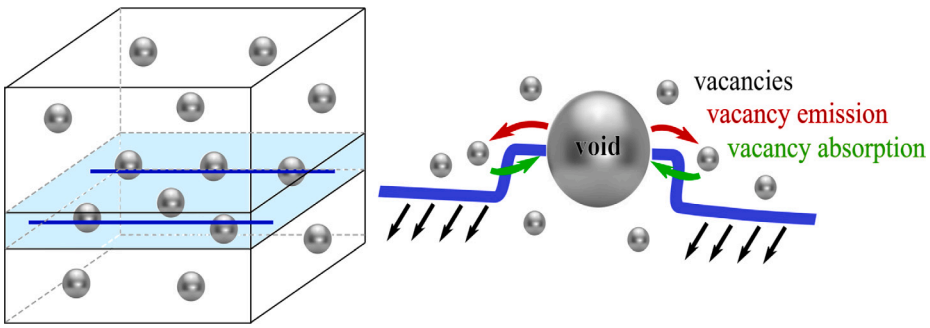

Fig. 21. Void shrink model.

the void center to the glide plane D_{vp} referred to the radius of void $1/2D_v$. This asymmetry comes from the nature of the stress field around an edge dislocation. During the interaction of a dislocation with a void, the stress concentration around the void is created. If the interaction volume is larger, higher stresses are required to move the dislocation past the void. When the dislocation crosses the void below its diameter, it interacts with a larger volume of material thus requiring a higher critical stress to unpin the dislocation. The possible interactions between dislocations and voids dictate the orientation of the primary glide planes for dislocation motion which intersect the voids at different angles (compare Fig. 20(c)). Dislocations move along these specific glide planes, and their interaction with voids is influenced by the proximity of the void relative to these planes and applied stress.

The value of critical stress should be related to different positions of the dislocation glide planes relative to the void center (compare Fig. 20(b)). The analysis leads to the conclusion that the critical stress necessary for unpinning the dislocation when crossing the void above its center (smaller part of the void is on the compressive side of the dislocation and larger part of the void is on the expansive side of the dislocation) is considerably lower than that required when passing through the center. It suggests that the radiation-induced void can undergo deformation and ultimately collapse into a dislocation loop, even at significantly reduced levels of critical stress.

Void shrink model

Void shrink model shown in Fig. 21 is based on another possible void deformation mechanism. During the interaction process between a dislocation and a large void, the dislocation on the glide plane absorbs the outermost vacancies from the void, making the void shrink (Landeiro Dos Reis et al., 2020). This model takes into account the volume change of the void caused by vacancies absorption and emission during the climb motion of an edge dislocation (Ji et al., 2022). The model assumes that the number of lost vacancies in a void is proportional to the void diameter.

The kinetic model to describe the evolution of void number density due to plastic deformation is proposed by Ji et al. (2022). The void evolution is determined based on the number of vacancies before and after the interaction with the dislocation denoted n_{vc} and n'_{vc}, respectively. The initial void volume is given as $n_{vc}\Omega = \pi D_v^3/6$, the updated void volume after the interaction of the void with the dislocation is expressed as $n'_{vc}\Omega = \pi(D'_v)^3/6$ and the vacancy volume is written as $\Omega = \pi d_{vc}^3/6$. The current void volume can be expressed as a difference between the initial void volume and the volume of lost vacancies

$$\frac{\pi D_v'^3}{6} = \frac{\pi D_v^3}{6} - \frac{\pi d_{vc}^3}{6}\alpha n_{vc}^{1/3} \tag{9}$$

where d_{vc} denotes the diameter of a single vacancy and α parameter is equal to 1.67 (Ji et al., 2022). This model assumes that the volume of absorbed vacancies is proportional to the void diameter and the one-third power of the total void volume $n_{vc} - n'_{vc} = \alpha n_{vc}^{1/3}$.

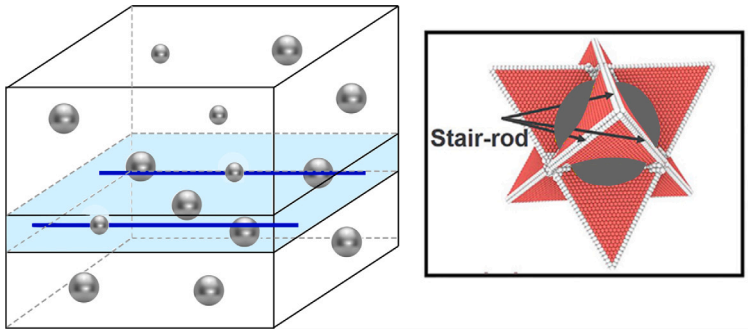

Fig. 22. Void collapse model; defect populations composed of two sizes of voids.

Finally, using the relation $n_{vc} = D_v^3/d_{vc}^3$, the above equation takes the form

$$\left(D_v'\right)^3 = D_v^3 - \alpha D_v d_{vc}^2 \tag{10}$$

To express the decrement of void diameter, the parameter of the proportion of the voids in the interaction is introduced as $D_v \Delta A/V$. Using Orowan relation, this term is expressed as a function of plastic strain as $D_v \Delta\gamma^p/b$. Thus, the reduction of void diameter is formulated in the following form

$$\Delta D_v = D_v - \left(D_v^3 - \alpha D_v d_{vc}^2 \frac{D_v \Delta\gamma^p}{b}\right)^{1/3} \tag{11}$$

where ΔA denotes the slip area increment of the dislocation (see Fig. 18).

Void collapse model

Void collapse model shown in Fig. 22 takes into consideration the defect population containing two sizes of voids, deforming according to two different mechanisms. The sizes of voids are chosen based on their relevance to the physical mechanisms responsible for plastic deformation. Larger vacancy clusters deform according to the mechanisms described in void cutting model and void shrink model (contraction of voids due to vacancies emission). Whereas, smaller voids cluster, during interaction with dislocation, collapse to the dislocation loop. The mechanism of void collapse is considered to gain a comprehensive description of the void deformation mechanisms (compare Guan et al., 2019). The incorporation of different void sizes is crucial as it reflects the heterogeneity effect on the radiation-induced nanovids behavior. This approach is supported by insights obtained from molecular dynamics (MD) simulations (compare Fig. 15), which provide a detailed understanding of the material's behavior at the atomic levels. The critical value of void diameter $D_{cr} = \eta_v^{1/2} d_{vc}$ is proposed to characterize and distinguish the different analyzed physical damage mechanisms of large and small voids, where the diameter of a single vacancy is denoted by d_{vc} and $\eta_v = 1.67$ is the efficiency of void collapse (Ji et al., 2022). Based on the critical parameter D_{cr}, the change in the average irradiation voids density N_v during the interaction in volume V is formulated in the following form

$$\Delta N_v = -\eta_v \alpha_v N_v b \frac{\Delta\gamma^p}{D_v} \quad \text{for} \quad D_{cr} < \eta_v^{1/2} d_{vc} \tag{12}$$

where α_v is a dimensionless coefficient reflecting voids barrier strength. For large voids, with a void diameter larger than D_{cr}, the mechanism of void cutting is implemented, as a result, the number of voids increases, and the void density will increase. For small voids containing only a few vacancy atoms, with a diameter smaller than D_{cr}, dislocations lead to the collapse of the void into the loop once they glide through the void density N_v will decrease. Void collapse model is based on the known initial density of voids N_v and their population. The voids density N_v can be determined during the process of collision cascades overlap (Fig. 2) or based on the void cutting model and updated during deformation process. Eq. (12) allows to determine the change in voids density as a result of their collapse into dislocation loops, provided that the size criterion for void $D_{cr} < \eta_v^{1/2} d_{vc}$ related to the diameter of a single vacancy d_{vc} is met.

Coupling effect between the density of voids and dislocation loops

The physical mechanism of void collapse leads to decrease in the population of voids and reduction of nanovoids density. Voids collapse into stair-rod dislocation loops thus the population of the loop increases. Thus, coupling effect between the density of voids and dislocation loop is identified. The relation between the density of voids N_v (defined as a voids number per unit volume, $(1/m^3)$) and dislocation loops N_l (defined as a total dislocation length per unit volume, (m/m^3)) express the coupling effect in the following form

$$\Delta N_l = \Delta N_v D_l = \eta_v \alpha_v N_v b \frac{\pi D_l}{D_v} \Delta\gamma^p, \quad \text{for} \quad D_{cr} < \eta_v^{1/2} d_{vc} \tag{13}$$

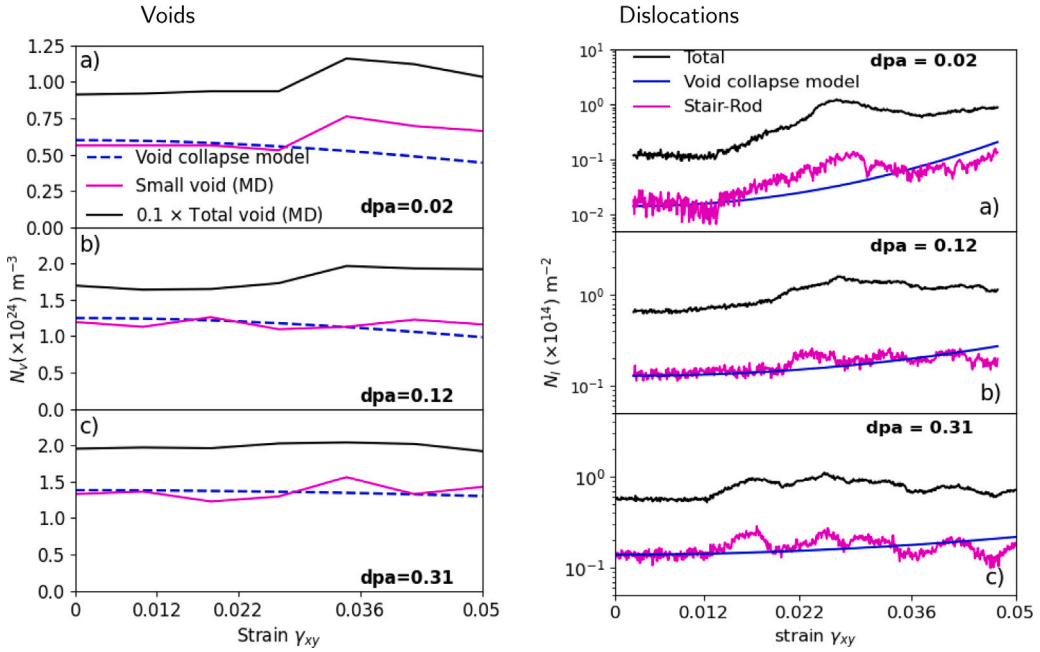

Fig. 23. The evolution of void and dislocation loops density as a function of shear strain for irradiated samples to different number of dpa. The solid line correspond to MD simulation results and the dashed represent the void collapse model. The total density of defects (voids or loops) is denoted by black solid line, pink solid line refers to density of small voids and stair-rod dislocation loops. (For interpretation of the references to color in this figure legend, the reader is referred to the web version of this article.)

where the scaling factor is the circumference of the dislocation loops πD_l. The mechanism of void collapse, expressed by the decreasing density of small voids ($D_v \approx D_{cr}$) and the corresponding increase in the displacement loop of the stair rod during plastic deformation is presented in Fig. 23. The evolution of void density (Fig. 23(A)) and dislocation loops density (Fig. 23(B)) are demonstrated as a function of shear strain for irradiated samples to different dpa values. The comparison between results obtained by MD simulations (solid lines) and that predicted by void collapse model (dashed line) is shown. The coupling effect between the density of voids and dislocation loops is clearly evident. Smaller sized voids collapse relatively quickly during deformation process. The decrease in the small void density (Fig. 23A), (pink solid line) corresponds to the increase in the density of stair-rod dislocation loops (Fig. 23B), (pink solid line). The physical mechanisms are independent of the dpa level, although the effect is best visible for a sample irradiated to dpa = 0.02. It is worth noting that the density fluctuations of small voids obtained with the multiple MD simulations are related to two physical processes, the mechanism of voids collapse (decrease of the voids density) and the increase of the voids density resulting from the aggregation of the singular vacancies occurring after irradiation into new voids (vacancy clusters). The mechanism of voids aggregation from vacancies is not included into the theoretical formulation, therefore it is not visible in the presented curves. The ensemble-average results from series of 50 MD simulations are used to generate the trends presented in Fig. 23. These results consistently represent the average behavior of the system under the given conditions.

6.2. Dislocations loops deformation

The hardening effect induced by interstitial loops can be well described through the dispersed barrier hardening (DBH) model (Bergner et al., 2014; Cui et al., 2018; Ji et al., 2022)

$$\tau_H^l = \alpha_l \mu b \sqrt{N_l^{tot}} \tag{14}$$

where τ_H^l represents the resolved shear stress necessary to unlock a dislocation from interstitial loops with total number density N_l^{tot} and average diameter D_l. α_l is a dimensionless coefficient reflecting defect barrier strength. The total number density of loops represents a sum $N_l^{tot} = N_l^{irr} + \Delta N_l^{vc}$ of radiation-induced loops N_l^{irr} and loops generated during voids collapse ΔN_l^{vc}.

Kinetic model of interstitial loops

The kinetic law for the evolution of density of radiation-induced dislocation loops due to plastic deformation is formulated in the following form

$$\Delta N_l^{tot} = -\lambda N_l^{tot} \frac{h\Delta A}{V} = -\lambda \left(N_l^{irr} + \Delta N_l^{vc}\right) \frac{h\Delta\gamma^p}{b} \tag{15}$$

Table 4
Parameters related to the hardening model. The Δ-parameter in our model was extracted by fitting the model to MD simulations of our material.

Parameter	Unit	Value
μ	[GPa]	80
b	Å	3.56
Δ	[–]	1.4182
n	[–]	0.5 (Ji et al., 2023)
n_c	[–]	2.22 (Ji et al., 2023)
α_v	[–]	5 for dpa = 0.02 4 for dpa = 0.12 1 for dpa = 0.31
α_l	[–]	$0.9 \cdot 10^{10}$ for dpa = 0.02 $0.025 \cdot 10^{11}$ for dpa = 0.12 $0.015 \cdot 10^{11}$ for dpa = 0.31
η_v	[–]	1.67 (Ji et al., 2023)

where λ is the defect annihilation fraction and h denotes the capture distance of irradiation defect clusters (Ji et al., 2022). Both radiation loops and those formed in the process of void collapse are evolving.

6.3. Irradiation hardening stress

The critical shear stress is additively decomposed into components that contribute to the hardening namely the critical stress related to the cluster of voids τ_v and dislocation loops τ_l

$$\tau_H^{n_c} = \left(\tau_H^v\right)^{n_c} + \left(\tau_H^l\right)^{n_c} \tag{16}$$

where $n_c = 2.22$ (Ji et al., 2022). This model can be directly used in micro and meso scale simulations, such as discrete dislocation dynamics (Pachaury et al., 2023; Chen et al., 2023) and crystal plasticity models (Liu et al., 2021; Pogorelko and Mayer, 2023; Das et al., 2020).

Fit parameters for each model are shown in Table 4.

6.4. Advantages and limitations of the proposed model

The proposed irradiation hardening model offers a detailed framework for understanding and predicting the effects of radiation on the mechanical properties of materials. By integrating physical mechanisms into the constitutive equations, the model captures the complex interactions between irradiation-induced defects and lattice defects. This section discusses the primary advantages and limitations of the model.

The main features of the proposed model are as follows:

- The model bridges phenomenological approach with physics-based formulations to advance fundamental understanding of physical mechanisms responsible for the plastic deformation of irradiated materials. The integration of the modified Bacon–Kocks–Scattergood (BKS) model for different void sizes enhances the model's capability to more accurately predict the critical resolved shear stress (CRSS), accounting for both strong and weak obstacles.
- The model is grounded in well-understood physical mechanisms governing the interaction of radiation-induced defects with lattice defects. By incorporating various mechanisms such as void cutting, void shrink, and void collapse, the model offers a more holistic view of the deformation of irradiated materials. That approach provides a theoretical foundation and increases the accuracy of predictions regarding irradiation hardening.
- The model's iterative character, where void characteristics such as diameter and density evolve with deformation, mirrors the dynamic changes occurring in irradiated materials. This approach ensures that the model can continuously adapt to ongoing changes in the material.
- Certain assumptions, such as the homogeneous distribution of voids during deformation, may not hold true in all cases. These simplifications can lead to discrepancies between model predictions and actual material behavior.
- The model primarily focuses on the interaction between dislocations and individual voids, but it does not fully account for the complex interactions between multiple voids or other types of radiation-induced defects like precipitates or interstitial clusters.
- Model requires precise material parameters (e.g., void size, spacing, and dislocation characteristics) for accurate predictions. Obtaining these parameters can be challenging and may limit the model's applicability in the absence of detailed material data.
- Extensive experimental validation and calibration against a wide range of irradiation conditions are required to ensure the model's accuracy and reliability.

In summary, the proposed irradiation hardening model presents a notable improvement in understanding and predicting the effects of irradiation on material properties, careful consideration of its limitations and refinement are necessary to fully harness its potential.

7. Concluding remarks

Understanding the evolution and interaction of radiation-induced defects under mechanical loads is of paramount importance for assessing the structural integrity and mechanical behavior of materials in radiation environments. These defects have a significant impact on the mechanical properties of the material, and knowledge of their evolution is crucial for predicting material performance and ensuring the safety and reliability of structural components in radiation-exposed environments, such as nuclear reactors and particle accelerator systems. The present study provides a deeper insight into the influence of radiation-induced defects on irradiation hardening. By analyzing the internal physical mechanisms, a better understanding of the behavior of irradiated materials is gained. In particular, a detailed physical analysis of the interaction between radiation-induced defects, such as voids and interstitial loops is conducted. These defects act as barriers to dislocation motion, leading to hardening and embrittlement. The study reveals various atomic-scale interaction mechanisms. In the case of voids, these mechanisms include pinning and unpinning, cutting of voids, void trapping, bowing of dislocation segments, and jog formation. For interstitial loops (e.g., Frank loops), the mechanisms involve pinning and unpinning, loop shearing, and loop absorption. The critical shear stress, which represents the stress required to initiate dislocation motion in the irradiated material, was thoroughly analyzed. It was found that irradiation increases the critical shear stress, making it more challenging for dislocations to move. This increase in critical shear stress is attributed to the interaction between radiation-induced defects and dislocations. Both voids and interstitial loops act as obstacles that pin or trap dislocations, impeding their motion. Notably, nanoscale voids present stronger barriers compared to dislocation loops of similar dimensions. Consequently, a higher stress level is necessary to overcome these obstacles and initiate dislocation motion. The critical shear stress serves as a crucial indicator of irradiation hardening. Moreover, in irradiated materials, plastic deformation is related to the mechanism of formation of defect-free channels. In dislocations channels, dislocations identify planes where they glide more easily, leading to the localization of plastic flow. As the process continues, dislocations interact with radiation-induced voids and loops, resulting in radiation hardening. Additionally, the interaction between radiation loops and dislocations leads to loop absorption or annihilation, resulting in a softening mechanism. Thus, the mechanism of voids cutting by dislocations contributes to additional hardening, while the collapse of voids and annihilation of dislocation loops lead to strain softening. These mechanisms seemingly oppose each other, but they coexist and determine the irradiated material's plastic behavior. These phenomena exist at the same time influenced by various factors such as radiation-induced voids and loops size and density, dislocations density, and their interaction. The plastic behavior of the material is determined by the combination of them. This demonstrates how intricate the relationship is between the behavior of radiation-induced defects and the plastic deformation of irradiated materials.

Finally, several new elements contained in the present paper can be summarized in the following way:

- Atomistic molecular dynamics (MD) simulations have been conducted in order to investigate the underlying mechanisms of interaction among radiation-induced defects, including voids and dislocation loops, that contribute to irradiation hardening.
- Irradiated alloys were prepared through overlapping cascade simulations in order to simulate the evolution of radiation–induced defects subjected to mechanical loads. The evolution of radiation defects (dislocation loops and voids) density during shear is determined.
- The physical mechanisms responsible for irradiation hardening in face-centered cubic alloy are explained. The mechanism of cutting the voids leads to increase of void density. The mechanism of void collapse contributed to the increasing dislocation loops density. The influence of the distance of the dislocation glide plane from the center of radiation-induced voids during dislocation-void interaction is analyzed.
- To capture identified irradiation hardening mechanisms the new hardening model for irradiated materials and the new kinetic laws for radiation void and the dislocation loops are formulated. The proposed model includes the coupling between the density of void and dislocation loops.
- Advanced experimental campaigns dedicated to irradiated materials were carried out to validate the MD simulations. Transmission electron microscopy (TEM) analyses were performed to confirm the structural changes resulting from ion irradiation and the interaction of defects, achieving good agreement with the MD simulation results.

CRediT authorship contribution statement

A. Ustrzycka: Writing – original draft, Visualization, Supervision, Methodology, Funding acquisition, Formal analysis, Data curation, Conceptualization. **F.J. Dominguez-Gutierrez:** Writing – original draft, Visualization, Software, Methodology, Formal analysis. **W. Chromiński:** Visualization, Validation, Data curation.

Declaration of competing interest

The authors declare that they have no known competing financial interests or personal relationships that could have appeared to influence the work reported in this paper.

Data availability

No data was used for the research described in the article.

Acknowledgments

This work is supported by the National Science Centre through Grant No UMO-2020/38/E/ST8/00453. FJDG (collision cascades) acknowledges support from the European Union Horizon 2020 research and innovation program under grant agreement no. 857470 and from the European Regional Development Fund via the Foundation for Polish Science International Research Agenda PLUS program grant No. MAB PLUS/2018/8. We acknowledge the computational resources provided by the Interdisciplinary Centre for Mathematical and Computational Modelling (ICM) University of Warsaw under computational allocation no g91–1427 and the CIS High Performance Cluster at the National Centre for Nuclear Research in Poland.

References

Bacon, D.J., Kocks, U.F., Scattergood, R.O., 1973. The effect of dislocation self-interaction on the orowan stress. Philos. Mag.: J. Theor. Exp. Appl. Phys. 28 (6), 1241–1263.

Bao, Q., Huang, M., Zhu, Y., Zhao, L., Li, Z., 2022b. Abnormal interactions between high-speed edge dislocation and microvoid in BCC metals. Int. J. Plast. 148, 103125, URL https://www.sciencedirect.com/science/article/pii/S0749641921001935.

Bao, Q., Li, Z., Zhu, B., Liang, S., Zhu, J., Huang, M., Zhao, L., Zhu, Y., 2023. Influence of kinetic effect on interaction between edge dislocation and irradiated dislocation loops in BCC tantalum. Int. J. Plast. 165, 103603, URL https://www.sciencedirect.com/science/article/pii/S074964192300089X.

Bao, H., Xu, H., Li, Y., Bai, H., Ma, F., 2022a. The interaction mechanisms between dislocations and nano-precipitates in CuFe alloys: A molecular dynamic simulation. Int. J. Plast. 155, 103317, URL https://www.sciencedirect.com/science/article/pii/S0749641922000997.

Barton, N., Arsenlis, A., Marian, J., 2013. A polycrystal plasticity model of strain localization in irradiated iron. J. Mech. Phys. Solids 61, 341–351.

Baudouin, J.-B., Nomoto, A., Perez, M., Monnet, G., Domain, C., 2015. Molecular dynamics investigation of the interaction of an edge dislocation with frank loops in Fe-Ni_{10}-Cr_{20} alloy. J. Nucl. Mater. 465, 301–310.

Beck, C.E., Hofmann, F., Eliason, J.K., Maznev, A.A., Nelson, K.A., Armstrong, D.E., 2017. Correcting for contact area changes in nanoindentation using surface acoustic waves. Scr. Mater. 128, 83–86, URL https://www.sciencedirect.com/science/article/pii/S1359646216304651.

Bergner, F., Pareige, C., Hernández-Mayoral, M., Malerba, L., Heintze, C., 2014. Application of a three-feature dispersed-barrier hardening model to neutron-irradiated Fe–Cr model alloys. J. Nucl. Mater. 448 (1), 96–102, URL https://www.sciencedirect.com/science/article/pii/S002231151400035X.

Bonny, G., Castin, N., Terentyev, D., 2013. Interatomic potential for studying ageing under irradiation in stainless steels: the FeNiCr model alloy. Modelling Simul. Mater. Sci. Eng. 21 (8), 085004.

Bonny, G., Terentyev, D., Pasianot, R.C., Poncé, S., Bakaev, A., 2011. Interatomic potential to study plasticity in stainless steels: the FeNiCr model alloy. Modelling Simul. Mater. Sci. Eng. 19, 085008.

Bryukhanov, I., 2020. Dynamics of edge dislocation in Cu–Ni solid solution alloys at atomic scale. Int. J. Plast. 135, 102834, URL https://www.sciencedirect.com/science/article/pii/S0749641920302254.

Chen, Y., Wang, S., Feng, H., Li, W., Liu, B., Li, J., Liu, Y., Liaw, P.K., Fang, Q., 2023. Irradiation hardening behavior of high entropy alloys using random field theory informed discrete dislocation dynamics simulation. Int. J. Plast. 162, 103497, URL https://www.sciencedirect.com/science/article/pii/S0749641922002741.

Cho, J., Molinari, J.-F., Anciaux, G., 2017. Mobility law of dislocations with several character angles and temperatures in FCC aluminum. Int. J. Plast. 90, 66–75, URL https://www.sciencedirect.com/science/article/pii/S0749641916303345.

Chrominski, W., Ciupinski, L., Bazarnik, P., Markelj, S., Schwarz-Selinger, T., 2021. Microstructure evolution in helium implanted self-irradiated tungsten annealed at 1700K studied by TEM. Mater. Charact. 174, 110991, URL https://www.sciencedirect.com/science/article/pii/S1044580321001212.

Cui, Y., Po, G., Ghoniem, N., 2017. Does irradiation enhance or inhibit strain bursts at the submicron scale? Acta Mater. 132, 285–297, URL https://www.sciencedirect.com/science/article/pii/S1359645417303476.

Cui, Y., Po, G., Ghoniem, N.M., 2018. A coupled dislocation dynamics-continuum barrier field model with application to irradiated materials. Int. J. Plast. 104, 54–67, URL https://www.sciencedirect.com/science/article/pii/S0749641917306964.

Das, S., Yu, H., Mizohata, K., Tarleton, E., Hofmann, F., 2020. Modified deformation behaviour of self-ion irradiated tungsten: A combined nano-indentation, HR-EBSD and crystal plasticity study. Int. J. Plast. 135, 102817, URL https://www.sciencedirect.com/science/article/pii/S0749641919308538.

Das, S., Yu, H., Tarleton, E., Hofmann, F., 2019. Hardening and strain localisation in helium-ion-implanted tungsten. Sci. Rep. 9, 18354.

Davila, L., Erhart, P., Bringa, E., Meyers, M., Lubarda, V., Schneider, M., Becker, R., Kumar, M., 2005. Atomistic modeling of shock-induced void collapse in copper. Appl. Phys. Lett. 86 (16).

Ding, M.-S., Tian, L., Han, W.-Z., Li, J., Ma, E., Shan, Z.-W., 2016. Nanobubble fragmentation and bubble-free-channel shear localization in helium-irradiated submicron-sized copper. Phys. Rev. Lett. 117, 215501, URL https://link.aps.org/doi/10.1103/PhysRevLett.117.215501.

Dominguez-Gutierrez, F., 2022. Temperature effects on the point defects formation in [111] W by neutron induced collision cascade. Nucl. Instrum. Methods Phys. Res. B 512, 38–41.

Dominguez-Gutierrez, F.J., Olejarz, A., Landeiro Dos Reis, M., Wyszkowska, E., Kalita, D., Huo, W.Y., Jozwik, I., Kurpaska, L., Papanikolaou, S., Alava, M.J., Muszka, K., 2024. Atomistic-level analysis of nanoindentation-induced plasticity in arc-melted NiFeCrCo alloys: The role of stacking faults. J. Appl. Phys. 135 (18), 185101.

Dominguez-Gutierrez, F.J., Ustrzycka, A., Xu, Q.Q., Alvarez-Donado, R., Papanikolaou, S., Alava, M.J., 2022. Dislocation nucleation mechanisms during nanoindentation of concentrated FeNiCr alloys: unveiling the effects of Cr through molecular simulations. Modelling Simul. Mater. Sci. Eng. 30 (8), URL www.scopus.com.

Doyle, P.J., Benensky, K.M., Zinkle, S.J., 2018. Modeling of dislocation channel width evolution in irradiated metals. J. Nucl. Mater. 499, 47–64, URL https://www.sciencedirect.com/science/article/pii/S0022311517312576.

Galitskiy, S., Mishra, A., Dongare, A.M., 2023. Modeling shock-induced void collapse in single-crystal Ta systems at the mesoscales. Int. J. Plast. 164, 103596, URL https://www.sciencedirect.com/science/article/pii/S0749641923000827.

Granberg, F., Nordlund, K., Ullah, M.W., Jin, K., Lu, C., Bei, H., Wang, L.M., Djurabekova, F., Weber, W.J., Zhang, Y., 2016. Mechanism of radiation damage reduction in equiatomic multicomponent single phase alloys. Phys. Rev. Lett. 116, 135504, URL https://link.aps.org/doi/10.1103/PhysRevLett.116.135504.

Guan, Y.-L., Dai, L.-S., Shao, J.-L., Song, W.-D., 2021. Molecular dynamics study on the nanovoid collapse and local deformation in shocked Cu50Zr50 metallic glasses. J. Non-Cryst. Solids 559, 120703, URL https://www.sciencedirect.com/science/article/pii/S0022309321000624.

Guan, Y.-L., Shao, J.-L., Song, W., 2019. Molecular dynamics study on nanoscale void collapse in single crystal aluminum under 1D and 3D compressions. Comput. Mater. Sci. 161, 385–393, URL https://www.sciencedirect.com/science/article/pii/S092702561930093X.

Hatano, T., Matsui, H., 2005. Molecular dynamics investigation of dislocation pinning by a nanovoid in copper. Phys. Rev. B 72, 094105, URL https://link.aps.org/doi/10.1103/PhysRevB.72.094105.

Hayakawa, S., Doihara, K., Okita, T., Itakura, M., Aichi, M., Suzuki, K., 2019. Screw dislocation–spherical void interactions in fcc metals and their dependence on stacking fault energy. J. Mater. Sci. 54, 11509–11525, Proceedings of the Second IEA Fusion Materials Agreement Workshop on Modeling and Experimental Validation.

Hirel, P., 2015. Atomsk: A tool for manipulating and converting atomic data files. Comput. Phys. Comm. 197, 212–219, URL https://www.sciencedirect.com/science/article/pii/S0010465515002817.
Hure, J., Shawish, S., Cizelj, L., Tanguy, B., 2017. Intergranular stress distributions in polycrystalline aggregates of irradiated stainless steel. J. Nucl. Mater. 492, 157–170.
Ji, C., Cui, Y., Li, Y., Ghoniem, N., 2022. A concurrent irradiation-mechanics multiscale coupling model. J. Mech. Phys. Solids 167, 105005, URL https://www.sciencedirect.com/science/article/pii/S0022509622001934.
Ji, C., Hu, J., Zhuang, Z., Cui, Y., 2023. Atomistically-informed hardening and kinetics models of helium bubble in irradiated tungsten. Int. J. Plast. 165, 103620, URL https://www.sciencedirect.com/science/article/pii/S0749641923001067.
Kocks, F., Mecking, H., 2003. Physics and phenomenology of strain hardening: The FCC case. Prog. Mater. Sci. 48, 171–273.
Krasnikov, V.S., Mayer, A.E., 2018. Influence of local stresses on motion of edge dislocation in aluminum. Int. J. Plast. 101, 170–187, URL https://www.sciencedirect.com/science/article/pii/S0749641917304503.
Kurpaska, L., Dominguez-Gutierrez, F., Zhang, Y., Mulewska, K., Bei, H., Weber, W., Kosińska, A., Chrominski, W., Jozwik, I., Alvarez-Donado, R., Papanikolaou, S., Jagielski, J., Alava, M., 2022. Effects of Fe atoms on hardening of a nickel matrix: Nanoindentation experiments and atom-scale numerical modeling. Mater. Des. 217, 110639, https://www.sciencedirect.com/science/article/pii/S026412752200260X.
Landeiro Dos Reis, M., Proville, L., Marinica, M.-C., Sauzay, M., 2020. Atomic scale simulations for the diffusion-assisted crossing of dislocation anchored by vacancy clusters. Phys. Rev. Mater. 4, 103603, URL https://link.aps.org/doi/10.1103/PhysRevMaterials.4.103603.
Landeiro Dos Reis, M., Proville, L., Sauzay, M., 2018. Modeling the climb-assisted glide of edge dislocations through a random distribution of nanosized vacancy clusters. Phys. Rev. Mater. 2, 093604, URL https://link.aps.org/doi/10.1103/PhysRevMaterials.2.093604.
Lehtinen, A., Granberg, F., Laurson, L., Nordlund, K., Alava, M., 2016. Multiscale modeling of dislocation-precipitate interactions in Fe: From molecular dynamics to discrete dislocations. J. Nucl. Mater. 93, 013309.
Levo, E., Granberg, F., Fridlund, C., Nordlund, K., Djurabekova, F., 2017. Radiation damage buildup and dislocation evolution in Ni and equiatomic multicomponent Ni-based alloys. J. Nucl. Mater. 490, 323–332, URL https://www.sciencedirect.com/science/article/pii/S0022311516313484.
Li, B., Wang, L., Ma, H., Luo, S., et al., 2014. Shock response of he bubbles in single crystal Cu. J. Appl. Phys. 116 (21).
dong Lin, P., feng Nie, J., peng Lu, Y., xin Shi, C., gang Cui, S., dong Cui, W., He, L., 2024. Atomic irradiation defects induced hardening model in irradiated tungsten based on molecular dynamics and CPFEM. Int. J. Plast. 103895, URL https://www.sciencedirect.com/science/article/pii/S0749641924000226.
Ling, C., Tanguy, B., Besson, J., Forest, S., Latourte, F., 2017. Void growth and coalescence in triaxial stress fields in irradiated FCC single crystals. J. Nucl. Mater. 492, 157–170.
Liu, J., 2015. Analysis of surface effects on the deformation of a nanovoid in an elasto-plastic material. Appl. Math. Model. 39 (17), 5091–5104, URL https://www.sciencedirect.com/science/article/pii/S0307904X15002346.
Liu, X.-Y., Biner, S., 2008. Molecular dynamics simulations of the interactions between screw dislocations and self-interstitial clusters in body-centered cubic Fe. Scr. Mater. 59 (1), 51–54, URL https://www.sciencedirect.com/science/article/pii/S1359646208001504.
Liu, J., Huang, M., Li, Z., Zhao, L., Zhu, Y., 2021. Microvoid growth mechanism in FCC polycrystals and a statistical damage model. Int. J. Plast. 137, 102888, URL https://www.sciencedirect.com/science/article/pii/S0749641920305076.
Liu, G., Wu, K., Yu, P., Cheng, X., Shi, J., Ye, C., Mao, Y., Shen, Y., 2023. Atomically-informed dislocation dynamics model for prediction of void hardening in irradiated tungsten. Int. J. Plast. 169, 103727, URL https://www.sciencedirect.com/science/article/pii/S0749641923002115.
Marian, J., Knap, J., Ortiz, M., 2005. Nanovoid deformation in aluminum under simple shear. Acta Mater. 53 (10), 2893–2900, URL https://www.sciencedirect.com/science/article/pii/S1359645405001497.
McElfresh, C., Cui, Y., Dudarev, S.L., Po, G., Marian, J., 2021. Discrete stochastic model of point defect-dislocation interaction for simulating dislocation climb. Int. J. Plast. 136, 102848, URL https://www.sciencedirect.com/science/article/pii/S0749641920304022.
Monnet, G., 2018. Multiscale modeling of irradiation hardening: Application to important nuclear materials. J. Nucl. Mater. 508, 609–627.
Monnet, G., Mai, C., 2019. Prediction of irradiation hardening in austenitic stainless steels: Analytical and crystal plasticity studies. J. Nucl. Mater. 518, 316–325, URL https://www.sciencedirect.com/science/article/pii/S002231151930056X.
Nordlund, K., Zinkle, S., Sand, A., Granberg, F., Averback, R., Stoller, R., Suzudo, T., Malerba, T., Banhart, F., Weber, W., Willaime, F., Dudarev, S., Simeone, D., 2018a. Improving atomic displacement and replacement calculations with physically realistic damage models. Nature Commun. 9, 1084.
Nordlund, K., Zinkle, S.J., Sand, A.E., Granberg, F., Averback, R.S., Stoller, R., Suzudo, T., Malerba, L., Banhart, F., Weber, W.J., Willaime, F., Dudarev, S.L., Simeone, D., 2018b. Primary radiation damage: A review of current understanding and models. J. Nucl. Mater. 512, 450–479.
Nowak, M., Mulewska, K., Azarov, A., Kurpaska, L., Ustrzycka, A., 2023. A peridynamic elasto-plastic damage model for ion-irradiated materials. Int. J. Mech. Sci. 237, 107806, URL https://www.sciencedirect.com/science/article/pii/S0020740322006865.
Osetsky, Y.N., 2021. Atomic-scale mechanisms of void strengthening in tungsten. Tungsten 3, 65–71.
Osetsky, Y., Bacon, D., 2003a. Void and precipitate strengthening in a-iron: what can we learn from atomic-level modelling? J. Nucl. Mater. 323 (2), 268–280, URL https://www.sciencedirect.com/science/article/pii/S0022311503003702. Proceedings of the Second IEA Fusion Materials Agreement Workshop on Modeling and Experimental Validation.
Osetsky, Y.N., Bacon, D.J., 2003b. An atomic-level model for studying the dynamics of edge dislocations in metals. Model. Simul. Mater. Sci. Eng. 11 (4), 427.
Osetsky, Y., Bacon, D., 2010. Atomic-scale mechanisms of void hardening in bcc and fcc metals. Phil. Mag. 90 (7–8), 945–961.
Pachaury, Y., Warren, G., Wharry, J.P., Po, G., El-Azab, A., 2023. Plasticity in irradiated FeCrAl nanopillars investigated using discrete dislocation dynamics. Int. J. Plast. 167, 103676, URL https://www.sciencedirect.com/science/article/pii/S0749641923001626.
Peng, X., Zhu, W., Chen, K., Deng, X., Wei, Y., 2016. Molecular dynamics simulations of void coalescence in monocrystalline copper under loading and unloading. J. Appl. Phys. 119 (16).
Pogorelko, V.V., Mayer, A.E., 2023. Dynamic tensile fracture of iron: Molecular dynamics simulations and micromechanical model based on dislocation plasticity. Int. J. Plast. 167, 103678, URL https://www.sciencedirect.com/science/article/pii/S074964192300164X.
Roach, A.M., Xu, S., Luscher, D.J., Gianola, D.S., Beyerlein, I.J., 2023. Interaction of extended dislocations with nanovoid clusters. Int. J. Plast. 168, 103684, URL https://www.sciencedirect.com/science/article/pii/S0749641923001705.
Rodney, D., 2004. Molecular dynamics simulation of screw dislocations interacting with interstitial frank loops in a model FCC crystal. Acta Mater. 52 (3), 607–614, URL https://www.sciencedirect.com/science/article/pii/S1359645403006128.
Rodney, D., Martin, G., Bréchet, Y., 2001. Irradiation hardening by interstitial loops: atomistic study and micromechanical model. Mater. Sci. Eng. A 309–310, 198–202, URL https://www.sciencedirect.com/science/article/pii/S0921509300017238. Dislocations 2000: An International Conference on the Fundamentals of Plastic Deformation.
Skoczeń, B., Ustrzycka, A., 2016. Kinetics of evolution of radiation induced micro-damage in ductile materials subjected to time-dependent stresses. Int. J. Plast. 80, 86–110, URL https://www.sciencedirect.com/science/article/pii/S0749641916000164?via.
Stukowski, A., 2009. Visualization and analysis of atomistic simulation data with OVITO–the open visualization tool. Modelling Simul. Mater. Sci. Eng. 18 (1), 015012.
Stukowski, A., 2010. Visualization and analysis of atomistic simulation data with OVITO-the open visualization tool. Model. Simul. Mater. Sci. Eng. 18 (1).
Tang, J., Xiao, J., Deng, L., Li, W., Zhang, X., Wang, L., Xiao, S., Deng, H., Hu, W., 2018. Shock wave propagation, plasticity, and void collapse in open-cell nanoporous Ta. Phys. Chem. Chem. Phys. 20 (44), 28039–28048.

Thompson, A.P., Aktulga, H.M., Berger, R., Bolintineanu, D.S., Brown, W.M., Crozier, P.S., in 't Veld, P.J., Kohlmeyer, A., Moore, S.G., Nguyen, T.D., Shan, R., Stevens, M.J., Tranchida, J., Trott, C., Plimpton, S.J., 2022. LAMMPS - a flexible simulation tool for particle-based materials modeling at the atomic, meso, and continuum scales. Comput. Phys. Comm. 271, 108171, URL https://www.sciencedirect.com/science/article/pii/S0010465521002836.

Tsugawa, K., Hayakawa, S., Iwase, Y., Okita, T., Suzuki, K., Itakura, M., Aichi, M., 2022. Molecular dynamics simulations to quantify the interaction of a rigid and impenetrable precipitate with an edge dislocation in Cu. Comput. Mater. Sci. 210, 111450, URL https://www.sciencedirect.com/science/article/pii/S0927025622002142.

Ustrzycka, A., Skoczen, B., Nowak, M., Kurpaska, L., Wyszkowska, E., Jagielski, J., 2020. Elastic–plastic-damage model of nano-indentation of the ion-irradiated 6061 aluminium alloy. Int. J. Damage Mech. 29, 1271–1305.

Vo, H., Frazer, D., Kohnert, A., Teysseyre, S., Fensin, S., Hosemann, P., 2023. Role of low-level void swelling on plasticity and failure in a 33 dpa neutron-irradiated 304 stainless steel. Int. J. Plast. 164, 103577, URL https://www.sciencedirect.com/science/article/pii/S0749641923000633.

Wang, Z., Yu, M., Long, X., Yang, C., Gao, N., Yao, Z., Wang, X., 2022. New mechanisms of dislocation line-loop interactions in BCC-Fe explored by molecular dynamics method. Results Phys. 34, 105226, URL https://www.sciencedirect.com/science/article/pii/S2211379722000377.

Williams, D.B., Carter, C.B., 2009. 1Transmission electron microscopy. In: A Textbook for Materials Science. Vol. 775, Springer New York, NY, p. LXII.

Wirth, B., Bulatov, V., Diaz de la Rubia, T., 2000. Atomistic simulation of stacking fault tetrahedra formation in Cu. J. Nucl. Mater. 283–287, 773–777, URL https://www.sciencedirect.com/science/article/pii/S0022311500002622. 9th Int. Conf. on Fusion Reactor Materials.

Wu, K., Liu, G., Yu, P., Ye, C., Shi, J., Shen, Y., 2022. Prediction of hardening effect by irradiation-induced vacancy clusters with dislocation dynamics. Int. J. Plast. 149, 103160, URL https://www.sciencedirect.com/science/article/pii/S0749641921002278.

Wyszkowska, E., Mieszczynski, C., Kurpaska, L., Azarov, A., Jozwik, I., Kosinska, A., Chrominski, W., Diduszko, R., Huo, W.Y., Cieslik, I., Jagielski, J., 2023. Tuning heterogeneous ion-radiation damage by composition in NixFe1-x binary single crystals. Nanoscale 15, 4870–4881.

Xiang, M., Cui, J., Yang, Y., Liao, Y., Wang, K., Chen, Y., Chen, J., 2017. Shock responses of nanoporous aluminum by molecular dynamics simulations. Int. J. Plast. 97, 24–45.

Xu, S., McDowell, D.L., Beyerlein, I.J., 2019. Sequential obstacle interactions with dislocations in a planar array. Acta Mater. 174, 160–172, URL https://www.sciencedirect.com/science/article/pii/S135964541930312X.

Yanilkin, A., Krasnikov, V., Kuksin, A., Mayer, A., 2014. Dynamics and kinetics of dislocations in Al and Al–Cu alloy under dynamic loading. Int. J. Plast. 55, 94–107, URL https://www.sciencedirect.com/science/article/pii/S0749641913001885.

Yu, P., Liu, G., Wu, K., Cui, Y., Zhao, G., Shen, Y., 2022. Exploring the effects of the sheared voids on the hardening of tungsten using atomistic simulations. J. Nucl. Mater. 562, 153548, URL https://www.sciencedirect.com/science/article/pii/S0022311522000447.

Zhang, Y., Zhao, S., Weber, W.J., Nordlund, K., Granberg, F., Djurabekova, F., 2017. Atomic-level heterogeneity and defect dynamics in concentrated solid-solution alloys. Curr. Opin. Solid State Mater. Sci. 21 (5), 221–237, URL https://www.sciencedirect.com/science/article/pii/S1359028616301565. Concentrated Solid Solution Alloys Perspective.

Ziegler, J.F., Ziegler, M., Biersack, J., 2010. SRIM – the stopping and range of ions in matter (2010). Nucl. Instrum. Methods Phys. Res. Sect. B 268, 1818–1823.

Zinkle, S.J., 2008. Microstructures and mechanical properties of irradiated metals and alloys. In: Ghetta, V., Gorse, D., Mazière, D., Pontikis, V. (Eds.), Materials Issues for Generation IV Systems. Springer Netherlands, Dordrecht, pp. 227–244.

Zinkle, S.J., Busby, J.T., 2009. Structural materials for fission and fusion energy. Mater. Today 12 (11), 12–19, URL https://www.sciencedirect.com/science/article/pii/S1369702109702949.